

Accelerated boundary integral method for multiphase flow in non-periodic geometries

Amit Kumar, Michael D. Graham*

Department of Chemical and Biological Engineering, University of Wisconsin-Madison, Madison, Wisconsin 53706, USA

Abstract

An accelerated boundary integral method for Stokes flow of a suspension of deformable particles is presented for an arbitrary domain and implemented for the important case of a planar slit geometry. The computational complexity of the algorithm scales as $O(N)$ or $O(N \log N)$, where N is proportional to the product of number of particles and the number of elements employed to discretize the particle. This technique is enabled by the use of an alternative boundary integral formulation in which the velocity field is expressed in terms of a single layer integral alone, even in problems with non-matched viscosities. The density of the single layer integral is obtained from a Fredholm integral equation of the second kind involving the double layer integral. Acceleration in this implementation is provided by the use of General Geometry Ewald-like method (GGEM) for computing the velocity and stress fields driven by a set of point forces in the geometry of interest. For the particular case of the slit geometry, a Fourier-Chebyshev spectral discretization of GGEM is developed. Efficient implementations employing the GGEM methodology are presented for the resulting single and the double layer integrals. The implementation is validated with test problems on the velocity of rigid particles and drops between parallel walls in pressure driven flow, the Taylor deformation parameter of capsules in simple shear flow and the particle trajectory in pair collisions of capsules in shear flow. The computational complexity of the algorithm is verified with results from several large scale multiparticle simulations.

Keywords: accelerated boundary integral, confined, slit, non-periodic, capsule, red blood cells, microfluidics, Chebyshev polynomials, influence matrix

1. Introduction

Multiphase flows in confined geometries is ubiquitous in nature and technological applications. A very common example is blood flow in the microcirculation. Recall that blood is primarily a suspension of red blood cells (RBCs) in plasma, with the volume fraction ϕ of RBCs (hematocrit) typically ranging between $\phi \sim 0.1 - 0.3$ in the capillaries and reaching as high as $\phi \approx 0.5$ in large arteries [11]. The diameter of the

*Corresponding author

Email address: graham@engr.wisc.edu (Michael D. Graham)

blood vessels in the microcirculation, which includes the capillaries, arterioles and venules, is typically in the range $10 - 125 \mu m$ [11], such that a discoidal RBC with a typical diameter and thickness of $8 \mu m$ and $2 \mu m$ respectively can be strongly to moderately confined. Therefore, any realistic computational study of blood flow in the capillaries must account for confinement. Other examples of technological interest where confinement effects are usually significant include multiphase flows in microfluidic devices [43]. Again, any realistic model must account for confinement in such problems. Given the importance of multiphase flows under confinement, or more generally speaking in non-periodic geometries, it is imperative to develop efficient and accurate computational techniques which faithfully represent the system under study, including the aspect of system size (meaning number of particles here). The algorithm presented herein has been motivated by our goal to study the class of problems described above. We next discuss some related previous efforts on the computational studies of multiphase flows under confinement.

Boundary integral based methods have emerged as a powerful tool for studying the flow behavior of multiphase systems in the limit of negligible Reynolds number, i.e. under Stokes flow conditions. Such methods have been employed in the past to study the flow behavior of a variety of particle types including drops, capsules, RBCs, and vesicles among others. Most of these prior implementations scale as $O(N^2)$, where N is proportional to the number of degrees of freedom in the system. For a system with N_p particles, each of which have been discretized into N_Δ elements, the number of degrees of freedom in the system scales as $N \sim N_p N_\Delta$. The $O(N^2)$ scaling above assumes an iterative solution of the discretized system of equations, where the number of iterations is independent of N ; a direct solution will result in a scaling of $O(N^3)$, while a system size dependent number of iterations with an iterative solution results in a scaling higher than $O(N^2)$; the worst case scaling being $O(N^3)$. The $O(N^2)$ scaling is usually prohibitive, such that it precludes a numerical study of large system sizes. It is therefore not surprising that many of the past studies have been limited to an $O(1)$ number of particles.

To overcome these limitations, there have been several efforts to develop *accelerated* techniques, where an accelerated technique is assumed to give a scaling closer to the ideal $O(N)$, while being sufficiently accurate at the same time. These accelerated techniques employ either some variant of the particle-particle-particle-mesh (P³M) method [6], or the Fast Multipole Method (FMM) [13]. One of the earliest Stokes flow boundary integral implementation with acceleration was perhaps presented by Greengard et al. [12], who employed the FMM for acceleration in complex domains. Using the particle-mesh-Ewald (PME) method, Metsi [31] developed an accelerated implementation of the Stokes flow boundary integral method for her studies on two dimensional periodic suspensions of emulsions and foams. Zinchenko and Davis [47, 48] employed multipole expansion accelerated boundary integral method to study large number of drops in a periodic geometry under shear. Freund [10] used the smooth particle-mesh-Ewald method to study the motion of periodic suspensions of RBCs and leukocytes in two dimensions; this was later extended to three dimensions by Zhao et al. [46]. In that study, the effect of confinement was incorporated by explicitly discretizing the walls,

which generally has unknown tractions and known no-slip velocity conditions. This explicit discretization is necessary because the periodic Green's function do not inherently satisfy the no-slip condition on the walls. Additionally, Zhao et al. [46] used a staggered time integrator, such the wall tractions and the particle surface velocities were not determined simultaneously; this is due to the large cost associated with their simultaneously solution. Another potential drawback with the periodic Green's function is that it has a zero mean flow (zero wave number component) and a non-zero mean pressure gradient associated with it [15]. As a consequence of this, the pressure drop in the system is not directly a specified quantity, and must be solved for by varying the mean flow, which is a specified quantity [10, 46]. Note that many experiments on pressure driven flow have a specified pressure drop, and it is therefore desired to specify the pressure drop directly in numerical simulations without incurring additional computational costs. In addition, we also note that the specified mean flow includes the flow outside the walls, as that is a part of the simulation box [46]; consequently, in such a formulation, neither the mean flow between the walls nor the pressure drop is a directly controlled quantity. Other recent work of possible interest is [37], where a FMM accelerated boundary integral method is presented. While this implementation was developed for an arbitrary domain, its applicability is restricted to two dimensional systems. In a subsequent article [45], the previous authors generalized their implementation to three dimensions, though only an unbounded domain was considered. At this point, it must be emphasized that all the prior accelerated implementations of the boundary integral method are based on either the free space Green's function or the periodic Green's function; in such a case, the boundaries of the confined domain are required to be explicitly discretized.

We next discuss previous boundary integral implementations employing the Green's function for the geometry of interest. Such a Green's function satisfies the appropriate boundary conditions at the domain boundaries; consequently, the unknowns at the domain boundaries, e.g. hydrodynamic tractions, do not enter the boundary integral equation. A popular geometry for which several boundary integral implementations have been developed is a slit – the region between two parallel walls. The Green's function for such a geometry has been provided by Liron and Mochon [28]; this has served as a basis of implementations described below. A boundary integral implementation based on this Green's function was developed by Staben et al. [42] for rigid particles. This was later extended by Griggs et al. [14] for studies on drops in the same geometry. In a related work, Janssen and Anderson [19] also implemented a boundary integral method for drops between two parallel walls, though that was restricted to matched continuous and dispersed phase viscosities. This was later extended by Janssen and Anderson [20] to include non-matched viscosity problems. It is important to emphasize that none of these implementations are accelerated and have a computational cost of at least $O(N^2)$. Consequently, it is not surprising that all of the studies described above were limited to a few particles and are thus not suitable for studying suspension dynamics.

We now briefly discuss examples of other numerical techniques employed in the literature for studies on the flow behavior of particles under confinement. One such simulation technique is the immersed boundary

method, which has been employed, e.g. by Doddi and Bagchi [8] and Pranay et al. [36], for studies on capsules in a slit. Another popular technique is the lattice-Boltzmann method. As an example, MacMeccan et al. [30] developed a coupled lattice-Boltzmann and finite element method to study deformable particles, which included studies under confinement. A somewhat related algorithm is the multiparticle collision dynamics, which has been used by, e.g., Noguchi and Gompper [33] to study RBCs and vesicles in capillaries. The ideal computational cost of all the above numerical techniques is $O(N)$.

In the present study, we develop an accelerated boundary integral method for an arbitrary geometry. The computational complexity of this algorithm scales as $O(N)$ or $O(N \log N)$ depending on the specific numerical scheme employed. The latter scaling of $O(N \log N)$ is associated with the use of fast Fourier transforms (FFTs) if one or more directions have periodic boundary conditions, though that is not a requirement of our method. In the present effort, we provide a detailed description using the example of the slit geometry; its extension to other geometries is straightforward. The acceleration in our method is obtained via the use of General Geometry Ewald-Like Method (GGEM), which provides fast point force solution to the Stokes equation in an arbitrary geometry [16]. This solution essentially provides the Green's function and other associated quantities in the geometry of interest; as a consequence, the confining geometry does not need to be explicitly represented and discretized in the boundary integral equation. In addition, as will be discussed later, the commonly employed boundary integral equation is not amenable to acceleration with GGEM, so we employ here an alternative formulation in which the velocity field is expressed solely in terms of a single layer integral involving only the Green's function [35]; its unknown density is obtained from a second kind integral equation involving the double layer integral. The resulting single and double layer integrals are computed efficiently employing the GGEM methodology, which results in the aforementioned favorable scaling of $O(N)$ or $O(N \log N)$.

The organization of this article is as follows. In Sec. (2), we introduce the boundary integral formulation and discuss its numerical implementation using GGEM. In Sec. (3), we describe the procedure to compute the hydrodynamic traction jump at a particle surface using the example of a capsule with a neo-Hookean membrane. We next provide extensive validation in Sec. (5), where we present results for several test problems and compare them to previous works. Lastly, in Sec. (6), we present results from several multiparticle simulations and also verify the computational complexity of our algorithm.

2. Problem Formulation and Implementation

2.1. Boundary integral equation for fluid motion

We consider a suspension of deformable particles (e.g. capsules) as shown in Fig. (1), where both the suspending fluid and the fluid enclosed by the particles are assumed to be Newtonian and incompressible. The viscosity of the suspending fluid is taken to be μ , while the viscosity of fluid enclosed by capsule m is taken to be $\lambda_m \mu$, such that λ_m is the viscosity ratio of the interior and the exterior fluid for this particular

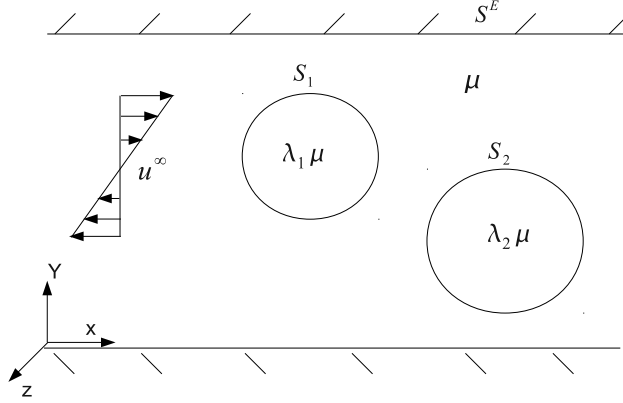


Figure 1: A schematic of the problem for Sec. (2.1). The figure shows the dispersed phase with viscosity μ inside the domain boundaries denoted by S^E . Also shown are two particles with internal viscosities $\lambda_1\mu$ and $\lambda_2\mu$ respectively; their surfaces are denoted by S_1 and S_2 . The undisturbed flow is denoted by \mathbf{u}^∞ .

capsule. The Reynolds number for the problem is assumed to be sufficiently small that fluid motion is governed by the Stokes equation. Under these assumptions, one may write the velocity at any point in the domain with an integral expression involving only the boundary of the particles [35]. We first introduce the formulation that is most commonly used,

$$\begin{aligned}
 u_j(\mathbf{x}_0) = & \frac{2}{1 + \lambda_m} u_j^\infty(\mathbf{x}_0) - \frac{1}{4\pi\mu(1 + \lambda_m)} \sum_{n=1}^{N_p} \int_{S^n} \Delta f_i(\mathbf{x}) G_{ji}(\mathbf{x}_0, \mathbf{x}) dS(\mathbf{x}) \\
 & + \frac{1}{4\pi(1 + \lambda_m)} \sum_{n=1}^{N_p} (1 - \lambda_n) \int_{S^n} u_i(\mathbf{x}) T_{ijk}(\mathbf{x}, \mathbf{x}_0) n_k(\mathbf{x}) dS(\mathbf{x}),
 \end{aligned} \tag{1}$$

where $\mathbf{u}(\mathbf{x}_0)$ is the fluid velocity at a point \mathbf{x}_0 lying on the boundary of a particle m (i.e. $\mathbf{x}_0 \in S^m$, S^m denoting the surface of particle m), $\mathbf{u}^\infty(\mathbf{x}_0)$ is the undisturbed fluid velocity at the point \mathbf{x}_0 , $\Delta \mathbf{f}(\mathbf{x})$ is the hydrodynamic traction jump across the interface [35], and the sums are over all the N_p particles in the system. The Green's function and its associated stress tensor are denoted by \mathbf{G} and \mathbf{T} respectively in the above equation, and integrals involving them as the kernel are typically referred to as the single layer integral and the double layer integral respectively [21, 35]. From here onwards, a principal value of the double layer integral over a part of the boundary is assumed whenever the target point \mathbf{x}_0 lies on that boundary. For example, in the above equation, the double layer integral over S^n is assumed to denote the principal value when $n = m$. A crucial aspect of the above formulation is that the Green's function \mathbf{G} and associated stress tensor \mathbf{T} are taken to satisfy the boundary conditions imposed at the system boundaries, so the integrals above only involve the internal (interfacial) boundaries; if the Green's function for any other geometry is employed (e.g. periodic), additional integrals over the domain boundaries arise in Eq. (1).

The above form of the boundary integral equation (1), using the free space Green's function (the Oseen-Burgers tensor) or the Green's function for a triply periodic cubic domain given by Hasimoto [15] is widely

used in the literature and is the basis for numerous numerical implementations, including the references cited in the introduction. However, for reasons that will be discussed shortly, this form is not amenable to numerical solution by an accelerated method in an arbitrary domain when using the Green's function for that domain. In the present effort, therefore, we employ an alternative formulation in which the fluid velocity is expressed solely in terms of the single layer integral with density $\mathbf{q}(\mathbf{x})$ as follows:

$$u_j(\mathbf{x}_0) = u_j^\infty(\mathbf{x}_0) + \sum_{n=1}^{N_p} \int_{S^n} q_i(\mathbf{x}) G_{ji}(\mathbf{x}_0, \mathbf{x}) dS(\mathbf{x}). \quad (2)$$

The single layer density $\mathbf{q}(\mathbf{x}_0)$ satisfies (for $\mathbf{x}_0 \in S^m$)

$$q_j(\mathbf{x}_0) + \frac{\kappa_m}{4\pi} n_k(\mathbf{x}_0) \sum_{n=1}^{N_p} \int_{S^n} q_i(\mathbf{x}) T_{jik}(\mathbf{x}_0, \mathbf{x}) dS(\mathbf{x}) = -\frac{1}{4\pi\mu} \left(\frac{\Delta f_j(\mathbf{x}_0)}{\lambda_m + 1} + \kappa_m f_j^\infty(\mathbf{x}_0) \right), \quad (3)$$

where κ_m is defined as

$$\kappa_m = \frac{\lambda_m - 1}{\lambda_m + 1}, \quad (4)$$

while \mathbf{f}^∞ is the traction at a given point (computed with the suspending fluid viscosity μ) due to the stress generated in the fluid corresponding to the undisturbed flow \mathbf{u}^∞ (see Appendix B for examples). In Appendix A, this formulation is derived from the Lorentz reciprocal theorem for the case of a single particle. This derivation follows closely the approach outlined in Chap. (5) of Pozrikidis [35] and is provided here for completeness.

We now clarify the motivation for employing Eqs. (2) and (3) rather than the more commonly employed formulation in Eq. (1). We begin by noting that the first argument \mathbf{x}_1 of $\mathbf{G}(\mathbf{x}_1, \mathbf{x}_2)$ and $\mathbf{T}(\mathbf{x}_1, \mathbf{x}_2)$ denotes the field (target) point of the functions, while the second argument \mathbf{x}_2 denotes the location of the pole (source) of the singularity that drives the flow. A close look at Eq. (1) reveals that the operand of $\mathbf{G}(\mathbf{x}_0, \mathbf{x})$, $\Delta f_i(\mathbf{x})$, is a function of the position of the pole of the singularity (\mathbf{x}) and that the field point of the \mathbf{G} tensor is same as the target point of the overall boundary integral equation (\mathbf{x}_0). In other words, the operand of \mathbf{G} is independent of its target point, and consequently the same collection of point forces can be used to compute the velocity at any target point. This requirement is essential to any accelerated method, as in such methods a part of the calculation gives the velocity (or other relevant quantities) simultaneously at *all* target points (e.g. boundary element nodes) due to *all* the singularities present in the system. This is possible only if the operands of the singularities are independent of the target points of the singularities, and instead are functions of the location of the pole of the respective singularities.

With this aspect clarified, it is seen that this important condition is not satisfied for the double layer kernel $\mathbf{T}(\mathbf{x}, \mathbf{x}_0)$ in Eq. (1) as its multiplicand $\mathbf{u}(\mathbf{x})$ and $\mathbf{n}(\mathbf{x})$ is a function of its target point \mathbf{x} . Also note that no general relationship exists that would allow one to switch the location of the pole and the field points in \mathbf{T} . (This is possible for \mathbf{G} , since, by self-adjointness, $G_{ij}(\mathbf{x}, \mathbf{x}_0) = G_{ji}(\mathbf{x}_0, \mathbf{x})$ [35].) Hence the

above formulation (1) is not suitable for our purposes here, though it can still be used for problems in which the viscosity ratio is unity, as the double layer integral vanishes in such a case [36]. In contrast, in the formulation employed in this work (Eqs. 2 and 3), the multiplicand $\mathbf{q}(\mathbf{x})$ of both $\mathbf{G}(\mathbf{x}_0, \mathbf{x})$ and $\mathbf{T}(\mathbf{x}_0, \mathbf{x})$ is a function of the source point of the singularity \mathbf{x} . Hence, it is amenable to numerical solution by an accelerated method.

We now describe the fast computation of the velocity and pressure fields due to a collection of known point forces, which is closely related to the problem of computing the Green's function and its associated stress tensor in the geometry of interest. Later in Secs. (2.4) and (2.5), we employ this technique to compute the single layer and double layer integrals.

2.2. GGEM Stokes flow solver for a collection of point forces

Consider the velocity field $\mathbf{u}(\mathbf{x})$ and the pressure field $p(\mathbf{x})$ due to a collection of N_s point forces, such that the strength and location of the ν^{th} point force are given by \mathbf{g}^ν and \mathbf{x}^ν respectively. The velocity and pressure fields above are obtained from the solution of the Stokes and the continuity equation as shown below:

$$-\nabla p(\mathbf{x}) + \mu \nabla^2 \mathbf{u}(\mathbf{x}) + \sum_{\nu=1}^{N_s} \mathbf{g}^\nu \delta(\mathbf{x} - \mathbf{x}^\nu) = 0, \quad (5a)$$

$$\nabla \cdot \mathbf{u}(\mathbf{x}) = 0, \quad (5b)$$

and subject to given boundary conditions on the system boundary S^E . By definition, the above velocity and pressure fields along with the associated stress tensor $\boldsymbol{\sigma}$ can be written in terms of a Green's function \mathbf{G} , its pressure vector \mathbf{P} and stress tensor \mathbf{T} as

$$u_i(\mathbf{x}) = \frac{1}{8\pi\mu} \sum_{\nu=1}^{N_s} G_{ij}(\mathbf{x}, \mathbf{x}^\nu) g_j^\nu, \quad (6a)$$

$$p(\mathbf{x}) = \frac{1}{8\pi} \sum_{\nu=1}^{N_s} P_j(\mathbf{x}, \mathbf{x}^\nu) g_j^\nu, \quad (6b)$$

$$\sigma_{ik}(\mathbf{x}) = \frac{1}{8\pi} \sum_{\nu=1}^{N_s} T_{ijk}(\mathbf{x}, \mathbf{x}^\nu) g_j^\nu. \quad (6c)$$

The stress tensor T_{ijk} in the above equation is obtained from G_{ij} and P_j from the Newtonian constitutive equation

$$T_{ijk}(\mathbf{x}, \mathbf{x}^\nu) = -P_j(\mathbf{x}, \mathbf{x}^\nu) \delta_{ik} + \mu \left(\frac{\partial G_{ij}(\mathbf{x}, \mathbf{x}^\nu)}{\partial x_k} + \frac{\partial G_{kj}(\mathbf{x}, \mathbf{x}^\nu)}{\partial x_i} \right). \quad (7)$$

A close look at the boundary integral equations (2) and (3) shows that to evaluate the integrals we do not explicitly need the Green's function \mathbf{G} and its stress tensor \mathbf{T} but only their products with the density \mathbf{q} . Put simply, our end goal is to efficiently (i.e. in a time that scales as $O(N)$ or $O(N \log N)$, where N is the

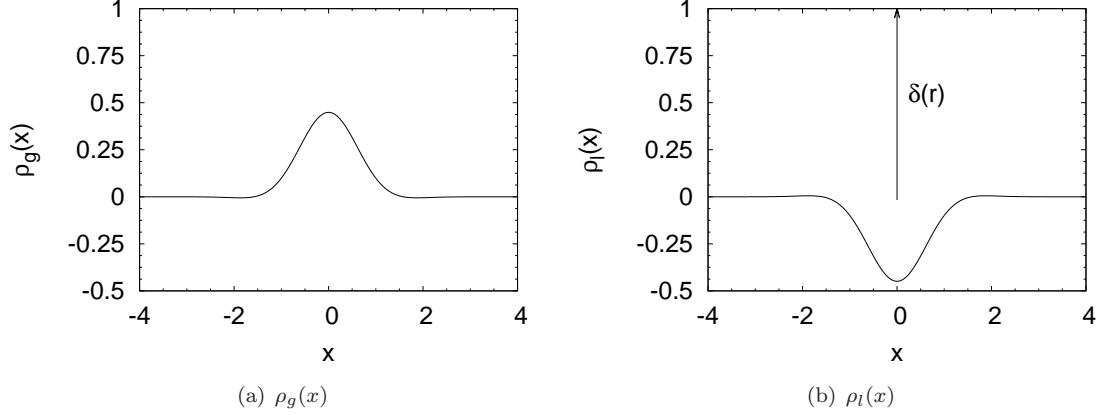


Figure 2: Variation of the global $\rho_g(x)$ and the local $\rho_l(x)$ force density along the x -axis, given the center of the force density is at the origin. Note that both of these densities are functions only of the distance r from the origin (see Eq. 8). Also note that $\rho_g(\mathbf{r}) + \rho_l(\mathbf{r}) = \delta(\mathbf{r})$. In numerical calculations, we set $\rho_g(\mathbf{r}) = 0$ for $r > 4/\alpha$. For plotting $\rho_g(x)$ and $\rho_l(x)$ here, we assumed $\alpha = 1$.

number of point forces in the system) find the velocity \mathbf{u} and the stress tensor $\boldsymbol{\sigma}$ due to a given set of point forces – explicit construction of \mathbf{G} and \mathbf{T} are not necessary.

One of the attractive features of the method presented here lies on the fact that it is applicable to an *arbitrary* geometry. For simplicity and considering the interest of the present work, we provide a detailed discussion only for a slit geometry (see Fig. 6); generalization of the formalism for an arbitrary geometry is straightforward [17]. For the present slit domain, there is a no slip boundary condition at the two rigid walls at $y = 0$ and $y = H$, while periodic boundary conditions are assumed in the other two directions x and z , with spatial periods L_x and L_z , respectively.

To achieve the computational complexity of $O(N \log N)$ alluded to above, we employ the general geometry Ewald like method (GGEM) [16] for computing the velocity and stress fields due to a given collection of point forces. We briefly describe GGEM next. We begin by expressing the Dirac-delta density in Eq. (5), as the sum of a smooth quasi-Gaussian *global* density $\rho_g(\hat{\mathbf{r}})$ and a second *local* density $\rho_l(\hat{\mathbf{r}})$ (see Fig. 2). These are respectively given by the following expressions

$$\rho_g(\hat{\mathbf{r}}) = \frac{\alpha^3}{\pi^{3/2}} e^{-\alpha^2 \hat{r}^2} \left(\frac{5}{2} - \alpha^2 \hat{r}^2 \right), \quad (8a)$$

$$\rho_l(\hat{\mathbf{r}}) = \delta(\hat{\mathbf{r}}) - \rho_g(\hat{\mathbf{r}}), \quad (8b)$$

where α^{-1} represents a length scale over which the delta-function density has been smeared using the quasi-Gaussian form above, and consequently it also represents the length scale beyond which both the global and the local densities are effectively zero, while $\hat{\mathbf{r}}$ is position vector relative to the pole of the singularity $\hat{\mathbf{r}} = \mathbf{x} - \mathbf{x}^\nu$. It is important to emphasize that the total density remains a δ -function, i.e. $\rho_g(\hat{\mathbf{r}}) + \rho_l(\hat{\mathbf{r}}) = \delta(\hat{\mathbf{r}})$. The motivation for this particular splitting of the δ -function density into $\rho_g(\hat{\mathbf{r}})$ and $\rho_l(\hat{\mathbf{r}})$ will be obvious

below.

We next consider the solution of the Stokes and continuity equation with the above two force densities as forcing functions. The solution driven by the local density, $\mathbf{u}^l(\mathbf{x})$, $p^l(\mathbf{x})$, and $\boldsymbol{\sigma}^l(\mathbf{x})$ (velocity, pressure, and stress respectively) will be referred to as the local solution, and satisfies the local problem

$$-\nabla p^l(\mathbf{x}) + \mu \nabla^2 \mathbf{u}^l(\mathbf{x}) + \sum_{\nu=1}^{N_s} \mathbf{g}^\nu \rho_l(\mathbf{x} - \mathbf{x}^\nu) = 0, \quad (9a)$$

$$\nabla \cdot \mathbf{u}^l(\mathbf{x}) = 0. \quad (9b)$$

This equation will be solved in an unbounded domain, i.e. the solution decays to zero at infinity. The solution $\mathbf{u}^g(\mathbf{x})$, $p^g(\mathbf{x})$, and $\boldsymbol{\sigma}^g(\mathbf{x})$ driven by the global density will be referred to as the global solution, and satisfies the global problem

$$-\nabla p^g(\mathbf{x}) + \mu \nabla^2 \mathbf{u}^g(\mathbf{x}) + \sum_{\nu=1}^{N_s} \mathbf{g}^\nu \rho_g(\mathbf{x} - \mathbf{x}^\nu) = 0, \quad (10a)$$

$$\nabla \cdot \mathbf{u}^g(\mathbf{x}) = 0. \quad (10b)$$

The boundary conditions for the global problem are set so that the total velocity field $\mathbf{u}(\mathbf{x}) = \mathbf{u}^l(\mathbf{x}) + \mathbf{u}^g(\mathbf{x})$ satisfies the specified boundary conditions for the overall problem. Once the local and the global solutions are known, the solution to the overall problem is obtained as

$$\mathbf{u}(\mathbf{x}) = \mathbf{u}^l(\mathbf{x}) + \mathbf{u}^g(\mathbf{x}), \quad (11a)$$

$$p(\mathbf{x}) = p^l(\mathbf{x}) + p^g(\mathbf{x}), \quad (11b)$$

$$\boldsymbol{\sigma}(\mathbf{x}) = \boldsymbol{\sigma}^l(\mathbf{x}) + \boldsymbol{\sigma}^g(\mathbf{x}). \quad (11c)$$

We next discuss the solution procedures for the local and the global problems.

2.2.1. Local solution

Consider first the local problem. The solution to this problem, $\mathbf{u}^l(\mathbf{x})$, $p^l(\mathbf{x})$, and $\boldsymbol{\sigma}^l(\mathbf{x})$ is expressed by a set of equations similar to that in Eqs (6), which, for the simplicity of nomenclature, is called the local Green's function \mathbf{G}^l and its associated quantities. In short, we append the superscript l to the previously defined quantities to denote the solution associated with the local density as the forcing function, and these are given by the following:

$$G_{ij}^l(\mathbf{x}, \mathbf{x}^\nu) = \left(\frac{\delta_{ij}}{\hat{r}} + \frac{\hat{x}_i \hat{x}_j}{\hat{r}^3} \right) \text{erfc}(\alpha \hat{r}) - \frac{2\alpha}{\sqrt{\pi}} \left(\delta_{ij} - \frac{\hat{x}_i \hat{x}_j}{\hat{r}^2} \right) e^{-\alpha^2 \hat{r}^2}, \quad (12a)$$

$$P_j^l(\mathbf{x}, \mathbf{x}^\nu) = \frac{2\hat{x}_j}{\hat{r}^3} \text{erfc}(\alpha \hat{r}) + \frac{4\alpha \hat{x}_j}{\sqrt{\pi}} \left(\frac{1}{\hat{r}^2} - \alpha^2 \right) e^{-\alpha^2 \hat{r}^2}, \quad (12b)$$

$$\begin{aligned}
T_{ijk}^l(\mathbf{x}, \mathbf{x}^\nu) = & -\frac{6\hat{x}_i\hat{x}_j\hat{x}_k}{\hat{r}^5}\text{erfc}(\alpha\hat{r}) - \frac{12\alpha}{\sqrt{\pi}}\frac{\hat{x}_i\hat{x}_j\hat{x}_k}{\hat{r}^4}e^{-\alpha^2\hat{r}^2} \\
& + \frac{4\alpha^3}{\sqrt{\pi}}\left(\delta_{jk}\hat{x}_i + \delta_{ik}\hat{x}_j + \delta_{ij}\hat{x}_k - \frac{2\hat{x}_i\hat{x}_j\hat{x}_k}{\hat{r}^2}\right)e^{-\alpha^2\hat{r}^2},
\end{aligned} \tag{12c}$$

where $\hat{\mathbf{x}} = \mathbf{x} - \mathbf{x}^\nu$, while $\hat{r} = |\hat{\mathbf{x}}|$. The velocity and stress fields are then obtained as:

$$u_i^l(\mathbf{x}) = \frac{1}{8\pi\mu} \sum_{\nu=1}^{N_s} G_{ij}^l(\mathbf{x}, \mathbf{x}^\nu) g_j^\nu, \tag{13a}$$

$$\sigma_{ik}^l(\mathbf{x}) = \frac{1}{8\pi} \sum_{\nu=1}^{N_s} T_{ijk}^l(\mathbf{x}, \mathbf{x}^\nu) g_j^\nu. \tag{13b}$$

The solution in Eq. (12) has been obtained with *free-space* boundary conditions, i.e. all of them decay to zero at infinity. In other words, the local solution is independent of the geometry of interest. The violation of the boundary condition requirements of the domain by employing free space boundary conditions above will be corrected by appropriately choosing the boundary conditions for the flow problem associated with the global force densities as the forcing function. An important observation at this point is that the local solutions in (12) are short ranged, decaying approximately as $e^{-\alpha^2\hat{r}^2}$. Consequently, the contribution from the local solution can be neglected beyond a length scale $\sim \alpha^{-1}$ from the origin of the corresponding local density. In this work, this cutoff length was taken as $r_{cut} = 4/\alpha$ throughout.

It is important to point out that the \mathbf{G}^l in Eq. (12a) has the same functional form as the real space term in the periodic Stokeslet (Green's function) provided by Hasimoto [15]. In other words, Hasimoto's solution for the periodic Stokeslet can also be obtained by first splitting the δ -function density into the local and global densities as in Eq. (8); the local problem is then solved as described above, while the global problem is solved with a Fourier Galerkin method with the appropriate assumptions described in Hasimoto [15]. Since PME accelerated methods (e.g. [22]) for Stokes flow employ the periodic Stokeslet given by Hasimoto [46], this observation illustrates a connection between PME like methods and GGEM. A very important distinction, though, is that the performance of PME like methods is tied to the use of discrete Fourier transforms and thus periodic domains, which is not the case with GGEM (discussed below), hence the latter's much broader applicability.

2.2.2. Global solution

We now describe the solution to the global problem, i.e. the flow problem associated with the collection of global force densities. We first discuss the boundary conditions for the global problem. As was mentioned earlier, the overall solution for a given collection of point forces is the sum of the corresponding quantities from the local and the global solutions, see Eq. (11). It is obvious that the same should be true for boundary conditions. Consequently, to satisfy any type of boundary condition (e.g. Dirichlet) at an arbitrary location, we set the boundary condition for the global part so that its sum with the known contribution from the

local part (above) adds up to the required value. Again, we employ the example of the slit geometry, noting that this scheme is equally applicable to other geometries. To satisfy the no-slip condition at the two rigid walls of the slit, we require the following at $y = 0$ and $y = H$:

$$\mathbf{u}^g = -\mathbf{u}^l. \quad (14)$$

Note that the *static* no-slip condition is always imposed at the rigid walls for computing the velocity field due to the Green's function (or point forces). This is true even in problems where the walls may not be at rest, a common example being shear flow. The effect of the undisturbed flow enters the boundary integral equation via \mathbf{u}^∞ and \mathbf{f}^∞ in Eqs. (2) and (3). To satisfy the periodic boundary conditions in x and z directions, we impose equivalent periodic boundary conditions in the global calculation. As far as the local solution is concerned, it is assumed that it decays to a negligible value over a length scale equal to half the spatial period in x and z directions, i.e. $r_{cut} < L_x/2$ and $r_{cut} < L_z/2$. Given the above choice $r_{cut} = 4/\alpha$, we require that $\alpha L_x > 8, \alpha L_z > 8$. This fact, coupled with the minimum image convention employed in the computation of the local solution ensures its periodicity.

With the boundary conditions for the global solution specified, we turn to the solution procedure of the Stokes and the continuity equation with the given collection of global force densities as the forcing function; see Eq. (10). For an arbitrary geometry one may employ any desired discretization scheme for the solution of the global problem. If a finite difference or a finite element scheme is used, then the solution can be obtained at a cost of $O(N)$ when the resulting sparse matrix equations are solved iteratively with proper preconditioners; the multigrid preconditioner for Stokes flow is an attractive choice [41, 9]. For the slit problem of interest here, past work [17, 36] employed discrete Fourier series approximation in the periodic x and z directions, while a second order finite difference discretization was employed in the wall normal y direction. In the present work, we develop a fully spectral solution procedure by employing the discrete Chebyshev polynomial approximation [3] in the wall normal direction, while the discrete Fourier series approximation is used in the periodic x and z directions. For example, the x -component u^g of the global velocity $\mathbf{u}^g = (u^g, v^g, w^g)$ in Eq. (10) is expressed as

$$u^g(\mathbf{x}) = \sum_{l=-N_x/2}^{N_x/2-1} \sum_{m=-N_z/2}^{N_z/2-1} \sum_{n=0}^{N_y-1} \hat{u}_{lmn}^g T_n(\bar{y}) e^{i2\pi lx/L_x} e^{i2\pi mz/L_z}, \quad (15)$$

where $T_n(\bar{y}) = \cos(n \cos^{-1} \bar{y})$ is the Chebyshev polynomial of the n^{th} degree [3], \bar{y} represents the mapping from $[0, H]$ to $[-1, 1]$: $\bar{y} = 2y/H - 1$, while N_x , N_y , and N_z respectively denote the number of terms (modes) in the corresponding series approximation. Similar expressions are written for other components of the velocity and the pressure. An important implication of this representation, particularly with regard to the pressure, is that the pressure drop associated with this point force solution is always zero over the spatial period of the domain, while the mean flow is (in general) non-zero. This ensures that the pressure drop

obtained from the boundary integral method always equals the pressure drop specified in the imposed bulk flow (i.e. in the absence of the particles). Returning to the expression in Eq. (15), we note that the use of the Fourier series approximation in x and z directions ensures that the periodic boundary conditions in these directions are inherently satisfied. The Chebyshev polynomials, on the other hand, do not automatically satisfy the boundary conditions in the wall normal direction; the satisfaction of these boundary conditions was accomplished by employing the tau method [3, 34]. In the tau method, the equations for the highest two modes in the series approximation are replaced by equations representing the two boundary conditions; see, e.g., Canuto et al. [3] or Peyret [34] for details. An attractive feature of the discrete Chebyshev polynomial approximation is that FFTs can be used for rapidly transferring information from the physical to spectral space and vice-versa [4]. A major drawback, though, with solving differential equations with Chebyshev polynomial approximation is that the differentiation matrix is full in both the spectral and the physical space [34] (in contrast, the Fourier differentiation matrix is diagonal in the spectral space). Due to the full nature of the Chebyshev differentiation matrix, a straightforward implementation for solving the Stokes flow problem will lead to an $O(N_y^3)$ method. For the incompressible Stokes flow problem here, though, an alternate approach exists in which the solution to the Stokes equation is obtained from the solution of a series of Helmholtz equations [4]. In this case, with little manipulation, a quasi-tridiagonal system of equations results, for which a direct $O(N_y)$ algorithm exists [34]. This approach for solving the incompressible Stokes equation, or more generally the incompressible Navier-Stokes equations, is popularly known in the literature as the Kleiser-Schumann influence matrix method [4]. A detailed discussion of this approach including the equations being solved and their respective boundary conditions is presented in Appendix C. Here we only sketch out the main computational aspects of this approach. To begin, each of variables appearing in the Stokes and the continuity equation are expanded in a truncated Fourier series in x and z directions; see, e.g., Eq. (15). These expressions are then substituted in the Stokes and the continuity equations. Subsequently, by the application of the Galerkin method, a set of coupled ordinary differential equations (ODE) in y is obtained for each of the Fourier modes of all the unknown variables (velocity components and pressure). These coupled ODEs are solved with the Chebyshev-tau influence matrix method, which involve Chebyshev transformations, quasi-tridiagonal matrix equation solves, and inverse Chebyshev transformations in that order. The solution thus obtained yields the Fourier coefficients of the velocity components and the pressure. An inverse Fourier transform then leads to the solution for the velocity and the pressure in the physical space. The computation of the stress tensor σ^g requires the derivatives of the velocities; these differentiations are performed in the transform space [3, 34]. All of the above Fourier and the Chebyshev transforms along with their inverse transforms are performed using the FFT algorithm. Thus, the asymptotic computational cost of the solution procedure for the global problem scales as $N \log N$, where $N = N_x N_y N_z$. A further discussion on the computational complexity of the algorithm is provided in Sec. (6.2).

We next introduce some of the important parameters associated with this solution procedure. Associated

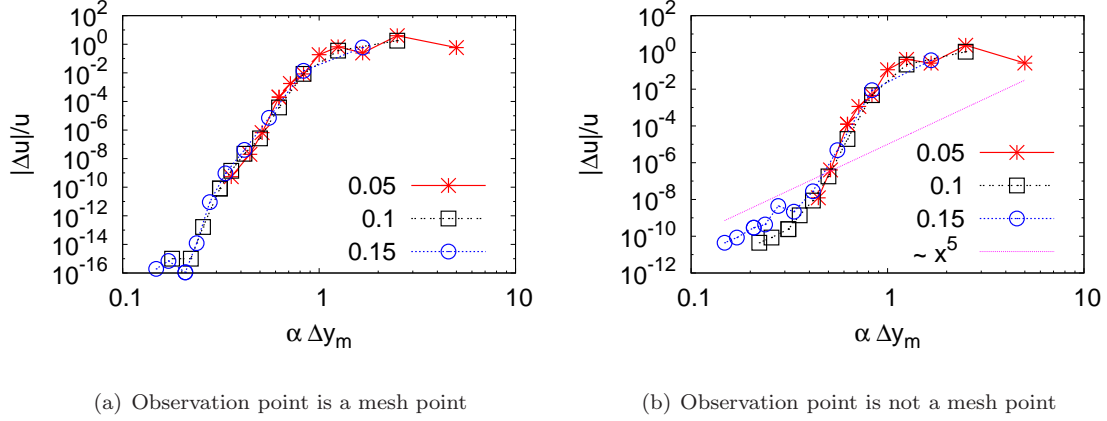


Figure 3: Relative error in the velocity ($\Delta u/u$) due to a point force at a given observation point in a slit geometry with $L_x = H = L_z = 1$. The abscissa in the plots is $\alpha \Delta y_m$, while the three different curves are for three different values of r_{cut} as labeled in the key. The strength of the point force considered is represented by the vector $(1, 1, 1)$ and its coordinates are $(0.25, 0.25, 0.25)$. (a) The observation point is $(0.5, 0.5, 0.5)$, which is always on a mesh point, and (b) the observation point is $(0.6312, 0.4734, 0.5234)$, which is not a mesh point.

with each of the N_x and N_z Fourier modes, there are N_x and N_z equispaced trapezoidal quadrature points; the corresponding spacings are denoted by $\Delta x_m = L_x/N_x$ and $\Delta z_m = L_z/N_z$. Similarly, associated with the N_y Chebyshev polynomials, there are N_y Chebyshev Gauss-Lobatto quadrature points, the j^{th} of which is given by $y_j = H/2(1 + \cos(\pi j/(N_y - 1)))$; the mean mesh spacing in this case is denoted by $\Delta y_m = H/(N_y - 1)$. Unless otherwise mentioned, the mean mesh spacings in all three directions are kept equal in simulations, i.e. $\Delta x_m = \Delta y_m = \Delta z_m$. For computing any of the above transforms, the value of the corresponding physical variable is required only at the corresponding quadrature points. Likewise, as is customary, the final solution for the velocity, pressure and stress are also computed only at these quadrature points. This last step is essential in maintaining the optimal computational complexity of $O(N \log N)$ alluded to above. The velocity and stress at any point not on the mesh is obtained via interpolation; here we employ 4^{th} order Lagrange interpolation for which the error decays as h^5 , where h is the characteristic mesh spacing. The error, therefore, is expected to decay exponentially fast with the number of modes for any point on the mesh, while it is expected to decay as h^5 for any point not on the mesh. We demonstrate this convergence behavior with a test problem in which a cubic slit is considered with the length of each side being unity, i.e. $L_x = L_z = H = 1$. A point force is placed at coordinates $(0.25, 0.25, 0.25)$ with its strength given by $(1, 1, 1)$. The velocity due to this point force is computed at the center of the box $(0.5, 0.5, 0.5)$, which is easy to keep on a mesh point. The solution is computed for three different values of $r_{cut} = 4/\alpha$: $r_{cut} = 0.05, 0.1$, & 0.15 . The relative error in the x component of the velocity $\Delta u/u$ is plotted against $\alpha \Delta y_m$ in Fig. (3a) for each value of r_{cut} . The data points in the plot for each r_{cut} were obtained by varying N_y between 17 and 181, while the solution computed with $N_y = 225$ and $r_{cut} = 0.15$ is taken as the reference for computing the error. As expected, the error in the velocity decays exponentially fast as $\alpha \Delta y_m$ is decreased; the convergence is

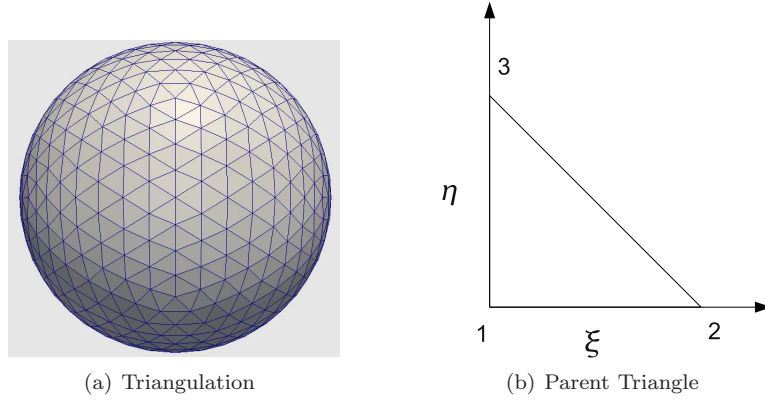


Figure 4: (a) Discretization of a sphere into triangular elements. The number of triangular elements and the number of vertices for the discretization shown in the figure are $N_{\Delta} = 1280$ and $N_b = 642$ respectively, (b) A schematic of the parent triangle. Edges 1-2 and 1-3 are of unit length.

ultimately limited by the machine precision, which is of $O(10^{-16})$ for double precision floating point numbers. Next we show the convergence in velocity at point with coordinates $(0.6312, 0.4734, 0.5234)$, which is unlikely to be a mesh point. The convergence in the velocity at this point is shown in Fig. (3b). In this case, too, an exponential convergence is initially observed as the value of $\alpha\Delta y_m$ is decreased, though, upon further decrease in $\alpha\Delta y_m$, the interpolation error dominates and a convergence as h^5 is obtained. An important point to note is that the exponential convergence is obtained only when the length scale of the global force density is well resolved by the mesh. Since the length scale of the global force density is represented by $r_{cut} \sim \alpha^{-1}$, the requirement for an exponential convergence is quantitatively expressed by the condition $\alpha\Delta y_m < 1$. This requirement on the mesh spacing is much easier to satisfy if one interprets $(\alpha\Delta y_m)^{-1}$ as the number of mesh points per unit smearing length represented by α^{-1} ; therefore the smaller is $\alpha\Delta y_m$, the higher is the resolution of the numerical scheme. Based on extensive numerical results presented here and later in this work, $\alpha\Delta y_m = 0.5$ is a recommended value as convergence was usually observed at this resolution.

2.3. Surface discretization

Having described the procedure for the fast computation of the velocity and the stress fields associated with a given collection of point forces, we now turn to the numerical solution of the boundary integral equation introduced in Sec. (2.1). In this section, we describe the discretization of the particle's surface into elements along with the basis functions employed over each element. Following this, we describe the numerical implementation of the single and the double layer integrals present in the boundary integral equation.

In this work, the surface of the capsule is discretized into triangular elements. Triangulation of a sphere is achieved by mapping the vertices of an icosahedron, which has 12 vertices and 20 triangular faces, to the surface of the inscribed sphere [39]. This procedure will, therefore, give 20 elements on the surface of the

sphere. Further refinement is obtained by subdividing each triangular face of the icosahedron recursively into 4 equal triangular elements, with all the vertices (and consequently the elements) again being mapped to the surface of the inscribed sphere as described above. The number of elements (N_Δ) and the number of vertices (N_b) obtained by this procedure can be expressed as $N_\Delta = 20 \cdot 4^k$ and $N_b = N_\Delta/2 + 2$, where k is the level of refinement ($k = 0$ corresponds to the original icosahedron). Note that the 12 original vertices of the icosahedron have a coordination number 5, while the remaining vertices have a coordination number of 6. As an example, a sphere subdivided into $N_\Delta = 1280$ elements with $N_b = 642$ vertices is shown in Fig. (4(a)).

2.3.1. Basis functions over elements

Linear basis functions are used over each element. All computations over a triangular element is performed by mapping to or from the parent triangle [18]. The parent triangle employed in this work is shown in Fig. (4(b)), where ξ and η denote the natural coordinates. The basis functions associated with the nodes 1, 2, and 3 are respectively given in natural coordinates by

$$\phi_1(\xi, \eta) = 1 - \xi - \eta, \quad (16a)$$

$$\phi_2(\xi, \eta) = \xi, \quad (16b)$$

$$\phi_3(\xi, \eta) = \eta. \quad (16c)$$

As an example, the position vector \mathbf{x} as a function of natural coordinates $\mathbf{x}(\xi, \eta)$ is obtained as

$$\mathbf{x}(\xi, \eta) = \phi_1(\xi, \eta) \mathbf{x}_1 + \phi_2(\xi, \eta) \mathbf{x}_2 + \phi_3(\xi, \eta) \mathbf{x}_3, \quad (17)$$

where \mathbf{x}_1 , \mathbf{x}_2 , and \mathbf{x}_3 are the real space positions of vertices 1, 2, and 3 respectively. The same procedure is employed to obtain the value of any physical variable (e.g. velocity) at coordinates (ξ, η) over the domain of the parent triangle.

2.4. Single layer integral

Let the single layer integral over the surface S be denoted by

$$w_j(\mathbf{z}) = \int_S q_i(\mathbf{x}) G_{ji}(\mathbf{z}, \mathbf{x}) dS(\mathbf{x}), \quad (18)$$

where $q_i(\mathbf{x})$ is the single layer density, while $\mathbf{w}(\mathbf{z})$ is assumed to represent the velocity at point \mathbf{z} . In order to employ GGEM as discussed in Sec. (2.2) to compute the above integral, we write this equation in the form

$$w_j(\mathbf{z}) = \int_S \int_V q_i(\mathbf{x}) \delta(\mathbf{y} - \mathbf{x}) G_{ji}(\mathbf{z}, \mathbf{y}) dS(\mathbf{x}) dV(\mathbf{y}), \quad (19)$$

where V represents the volume of the domain and δ is the three dimensional Dirac-delta function. It is easy to see that both the expressions for $\mathbf{w}(\mathbf{z})$ in Eqs. (18) and (19) are identical. Next, we write the Dirac-delta

function as a sum of the local and the global density introduced in Sec. (2.2); see Eq. (8). Consequently, we have

$$w_j(\mathbf{z}) = \int_S \int_V q_i(\mathbf{x}) (\rho_l(\mathbf{y} - \mathbf{x}) + \rho_g(\mathbf{y} - \mathbf{x})) G_{ji}(\mathbf{z}, \mathbf{y}) dS(\mathbf{x}) dV(\mathbf{y}), \quad (20)$$

Next, we separate the integrals associated with the local and global densities, and write the contribution due to the local density as

$$w_j^l(\mathbf{z}) = \int_S q_i(\mathbf{x}) \left(\int_V \rho_l(\mathbf{y} - \mathbf{x}) G_{ji}(\mathbf{z}, \mathbf{y}) dV(\mathbf{y}) \right) dS(\mathbf{x}). \quad (21)$$

It is easy to see that the above integral can be written as

$$w_j^l(\mathbf{z}) = \int_S q_i(\mathbf{x}) G_{ji}^l(\mathbf{z}, \mathbf{x}) dS(\mathbf{x}), \quad (22)$$

where \mathbf{G}^l has been defined in Eq. (12). This follows from the fact that the local Green's function $\mathbf{G}^l(\mathbf{z}, \mathbf{x})$ can also be constructed by the superposition of Green's function $\mathbf{G}(\mathbf{z}, \mathbf{y})$ weighted by the density $\rho^l(\mathbf{y} - \mathbf{x})$, i.e.

$$G_{ji}^l(\mathbf{z}, \mathbf{x}) = \int_V \rho_l(\mathbf{y} - \mathbf{x}) G_{ji}(\mathbf{z}, \mathbf{y}) dV(\mathbf{y}). \quad (23)$$

It is important to emphasize that the domain was assumed to be unbounded in arriving at Eq. (23). This is *always* the case for the local problem as discussed in Sec. (2.2); any error in the boundary condition introduced due to this assumption will be accounted for in the global calculation. Next, consider the contribution from the global density in Eq. (20), which we write as

$$w_j^g(\mathbf{z}) = \int_S \int_V q_i(\mathbf{x}) \rho_g(\mathbf{y} - \mathbf{x}) G_{ji}(\mathbf{z}, \mathbf{y}) dV(\mathbf{y}) dS(\mathbf{x}). \quad (24)$$

It can shown that $\mathbf{w}^g(\mathbf{z})$ satisfies

$$-\nabla p^{w^g}(\mathbf{z}) + \mu \nabla^2 \mathbf{w}^g(\mathbf{z}) + \mu \mathbf{\Pi}^g(\mathbf{z}) = 0, \quad (25a)$$

$$\nabla \cdot \mathbf{w}^g(\mathbf{z}) = 0, \quad (25b)$$

where the density $\mathbf{\Pi}^g(\mathbf{z})$ is given by

$$\mathbf{\Pi}^g(\mathbf{z}) = 8\pi \int_S \mathbf{q}(\mathbf{x}) \rho_g(\mathbf{z} - \mathbf{x}) dS(\mathbf{x}). \quad (26)$$

The boundary condition for the global solution comes from the known local solution ($\mathbf{w}^l(\mathbf{z})$ for \mathbf{z} at the domain boundary) and the given overall boundary conditions, such that the sum of the local and the global solution satisfies the overall boundary condition; see Sec. (2.2). Having expressed the single layer integral in a form suitable for its computation with the GGEM technique, we next describe its numerical implementation. This includes the numerical solution of the local problem represented by Eq. (22) and the global problem represented by Eq. (25).

2.4.1. Local contribution

We first consider the contribution from the local Green's function to the velocity at a given point \mathbf{z} , which typically is one of the nodes of the elements. We discretize the surface integral in Eq. (22) as

$$w_j^l(\mathbf{z}) = \sum_{k=1}^{N_\Delta} \int_{S_k} q_i(\mathbf{x}) G_{ji}^l(\mathbf{z}, \mathbf{x}) dS(\mathbf{x}), \quad (27)$$

where the summation is over all the triangular elements N_Δ representing the surface S , while S_k denotes an integral over the element k . For convenience, all the integrals are performed over the parent triangle. To accomplish this, we write the above equation as

$$w_j^l(\mathbf{z}) = \sum_{k=1}^{N_\Delta} \int_0^1 \int_0^{\xi(\eta)} q_i(\mathbf{x}(\xi, \eta)) G_{ji}^l(\mathbf{z}, \mathbf{x}(\xi, \eta)) \omega d\xi d\eta, \quad (28)$$

where the differential area element dS has been replaced by its equivalent expression

$$dS = \omega d\xi d\eta = |\mathbf{x}_\xi \times \mathbf{x}_\eta| d\xi d\eta. \quad (29)$$

As noted earlier, the value of any quantity can be obtained at coordinates (ξ, η) by the usual interpolation from the corresponding values at the nodes of the triangle, e.g. see Eq. (17). The double integral in Eq. (28) is evaluated using the product of two one-dimensional Gauss-Legendre quadrature rule (one for ξ and the other for η). This proved competitive in terms of computational cost for a given accuracy with Gaussian quadrature rules available for a triangular element [18], perhaps due to the fact that the integrands are not polynomials. In most cases a 4x4 product rule is found to be sufficient for accurate integration over a triangular element. In addition, if the vertex at which the velocity is being computed is a member of the triangular element over which the integration is being performed, then the integral in Eq. (28) over the parent triangle is further transformed to polar coordinates (r, θ) [39]. This transformation makes the integrand non-singular and hence ensures sufficient accuracy with the same low order product integration rule discussed above. Lastly, we note that for computing the contribution to velocity at any given point \mathbf{z} due to the local Green's function, only triangular elements within a distance of $r_{cut} \sim \alpha^{-1}$ from the point \mathbf{z} need to be considered. This is justified due to the exponentially decaying contribution from the integral over an element at separations larger than $O(\alpha^{-1})$ from the point of interest.

2.4.2. Global Contribution

Our goal here is to find $\mathbf{\Pi}^g(\mathbf{z})$ in Eq. (25), for which we need to compute the integral in Eq. (26). We being by discretizing the integral in Eq. (26) and write it as

$$\mathbf{\Pi}^g(\mathbf{z}) = \sum_{k=1}^{N_\Delta} \int_{S_k} q_i(\mathbf{x}) \rho_g(\mathbf{z} - \mathbf{x}) dS(\mathbf{x}). \quad (30)$$

The above integral can be evaluated with any desired quadrature rule, though, due to the smoothly varying nature of the integrand a simple trapezoidal rule proves sufficient. Note that the trapezoidal integration rule essentially reassigns the contribution from the surface of the triangular element to its three vertices in equal proportions. Consider first the integral over an element S_k in Eq. (30), which as per the trapezoidal rule is expressed as a sum of contributions from its three vertices as

$$[\Pi_i^g(\mathbf{z})]_{S_k} = \sum_{p=1}^3 \left(\frac{A_k q_i(\mathbf{x}^{k_p})}{3} \right) \rho_g(\mathbf{z} - \mathbf{x}^{k_p}), \quad (31)$$

where A_k is the area of the triangular element S_k , p denotes the vertex number of the given element k , \mathbf{x}^{k_p} denotes the coordinate of the p^{th} vertex of the triangular element k , and $[\Pi^g(\mathbf{z})]_{S_k}$ denotes the density at \mathbf{z} due to the integration over the element S_k only. The term in the parenthesis in Eq. (31) can be considered as the strength of the global density at the node \mathbf{x}^{k_p} due to the element k ; by summing it over all the elements k to which a given node belongs (let us say that this node is *globally* represented by \mathbf{x}^b), one obtains the total strength of the global density at this node, say \mathbf{q}^b . The overall density at a point \mathbf{z} is then obtained by adding contributions from all the nodes present in the system,

$$\Pi_i^g(\mathbf{z}) = \sum_{p=1}^{N_b} q_i^b \rho_g(\mathbf{z} - \mathbf{x}^b), \quad (32)$$

where N_b is the total number of nodes in the system. We also note that due to the exponentially decaying nature of $\rho_g(\mathbf{z} - \mathbf{x}^b)$ as a function of separation from \mathbf{x}^b , to compute the density at a point \mathbf{z} one only considers those nodes which are within a distance $r_{cut} \sim \alpha^{-1}$ from the point. Once $\Pi^g(\mathbf{z})$ is evaluated, we solve the set of equations in (25) using the procedure described in detail in Sec. (2.2). This gives us $\mathbf{w}^g(\mathbf{z})$, which upon addition to the local contribution $\mathbf{w}^l(\mathbf{z})$ gives the overall single layer integral $\mathbf{w}(\mathbf{z})$, i.e.

$$\mathbf{w}(\mathbf{z}) = \mathbf{w}^l(\mathbf{z}) + \mathbf{w}^g(\mathbf{z}). \quad (33)$$

2.5. Double layer integral

We now describe the evaluation of the double layer integral. We denote the double layer integral over a surface S (similar to that in Eq. 3) by

$$v_j(\mathbf{z}) = n_k(\mathbf{z}) \int_S q_i(\mathbf{x}) T_{jik}(\mathbf{z}, \mathbf{x}) dS(\mathbf{x}). \quad (34)$$

If we define a stress tensor $\boldsymbol{\sigma}(\mathbf{z})$ as (note that one needs to multiply it by μ to get units of stress)

$$\sigma_{jk}(\mathbf{z}) = \int_S q_i(\mathbf{x}) T_{jik}(\mathbf{z}, \mathbf{x}) dS(\mathbf{x}), \quad (35)$$

then we have the following relationship between $\mathbf{v}(\mathbf{z})$ and $\boldsymbol{\sigma}(\mathbf{z})$:

$$v_j(\mathbf{z}) = n_k(\mathbf{z}) \sigma_{jk}(\mathbf{z}). \quad (36)$$

The motivation for introducing the stress field $\boldsymbol{\sigma}(\mathbf{z})$ in Eq. (35) should be clear now, as it is the stress field associated with the following velocity field

$$w_j(\mathbf{z}) = \int_S q_i(\mathbf{x}) G_{ji}(\mathbf{z}, \mathbf{x}) dS(\mathbf{x}). \quad (37)$$

As described in the previous section (2.4), we write the above velocity field as the sum of a local $\mathbf{w}^l(\mathbf{z})$ and global $\mathbf{w}^g(\mathbf{z})$ velocity fields, and denote the corresponding stress fields by $\boldsymbol{\sigma}^l(\mathbf{z})$ and $\boldsymbol{\sigma}^g(\mathbf{z})$ respectively. Using (36), we obtain the corresponding local and global contributions to the double layer integral as

$$v_j^l(\mathbf{z}) = n_k(\mathbf{z}) \sigma_{jk}^l(\mathbf{z}), \quad (38a)$$

$$v_j^g(\mathbf{z}) = n_k(\mathbf{z}) \sigma_{jk}^g(\mathbf{z}). \quad (38b)$$

We describe the computation of the global contribution to the double layer integral first, as it is a straightforward extension of the procedure presented in Sec. (2.4). This will be followed by a discussion of the procedure for computing the local contribution to the double layer integral.

2.5.1. Global contribution

Here we describe the procedure to compute the global contribution to the double layer integral. Consider the global velocity field $\mathbf{w}^g(\mathbf{z})$ and the pressure field $p^{w^g}(\mathbf{z})$ associated with the global force density $\boldsymbol{\Pi}^g(\mathbf{z})$; see Eq. (25). The procedure to compute the velocity and pressure field for this *global* distribution of density has been discussed in detail in Sec. (2.4). Once these are known, one can obtain the stress field $\boldsymbol{\sigma}^g(\mathbf{z})$ from the usual Newtonian constitutive equation as

$$\sigma_{jk}^g(\mathbf{z}) = -\frac{p^{w^g}(\mathbf{z})}{\mu} \delta_{jk} + \left(\frac{\partial w_j^g(\mathbf{z})}{\partial x_k} + \frac{\partial w_k^g(\mathbf{z})}{\partial x_j} \right). \quad (39)$$

As was mentioned in Sec. (2.2), the differentiations required in the above expression are performed in the transform space [3, 34]; consequently, the stress field is known with spectral accuracy at the mesh points. Once the stress tensor is obtained at the mesh points, the stress at the nodes of the elements are obtained using 4th order Lagrange interpolation. Lastly, $\mathbf{v}^g(\mathbf{z})$ is obtained from Eq. (38b).

2.5.2. Local contribution

Consider the velocity field due to the local density, which is written as

$$w^l(\mathbf{z}) = \int_S q_i(\mathbf{x}) G_{ji}^l(\mathbf{z}, \mathbf{x}) dS(\mathbf{x}). \quad (40)$$

It is trivial to show that the stress field associated with the above velocity field is given by the following

$$\sigma_{jk}^l(\mathbf{z}) = \int_S q_i(\mathbf{x}) T_{jik}^l(\mathbf{z}, \mathbf{x}) dS(\mathbf{x}), \quad (41)$$

and consequently the local contribution to the double layer integral is given by

$$v_j^l(\mathbf{z}) = n_k(\mathbf{z}) \int_S q_i(\mathbf{x}) T_{jik}^l(\mathbf{z}, \mathbf{x}) dS(\mathbf{x}). \quad (42)$$

The above integral is discretized in the same fashion as in Sec. (2.4), and is written as a sum of integrals over the triangular elements. Again, as in Sec. (2.4.1), all the integrals are performed over the parent triangle as follows

$$v_j^l(\mathbf{z}) = n_k(\mathbf{z}) \sum_{k=1}^{N_\Delta} \int_0^1 \int_0^{\xi(\eta)} q_i(\mathbf{x}(\xi, \eta)) T_{jik}^l(\mathbf{z}, \mathbf{x}(\xi, \eta)) \omega d\xi d\eta. \quad (43)$$

The integral in the above equation is performed with the product of two one dimensional Gauss-Legendre quadrature rule; see Sec (2.4.1) for details. When the vertex at \mathbf{z} is a member of the element over which integration is performed, the integrand is singular and requires special treatment. At this point it is worth noting that the double layer integrand has the same $1/\hat{r}$ singularity as the single layer integral [32], as $\hat{\mathbf{x}} \cdot \mathbf{n}(\mathbf{x}_0) \approx \hat{r}^2$ for small \hat{r} . So in principle one may employ the polar coordinate transformation to regularize the singular double layer integral. In practice, because we employ flat elements, the condition $\hat{\mathbf{x}} \cdot \mathbf{n}(\mathbf{x}_0) \approx \hat{r}^2$ is not valid. Note that the normal vector at any given vertex is taken as the area averaged normal vector of triangles to which it belongs, from which it follows that the numerical double layer has a $1/\hat{r}^2$ singularity.

In the literature, desingularization of the double layer integral is usually achieved by singularity subtraction [35]. This desingularization scheme is also applicable for the current formulation (34), though this desingularization procedure would require 9 times the computational effort of performing the double layer integral itself; we omit the details here. We therefore look elsewhere for more computationally efficient schemes for performing the singular part of the double layer integral. The first point to note is that the singularity in the stress tensor associated with the Green's function $\mathbf{T}(\mathbf{z})$ is entirely contained in the local part $\mathbf{T}^l(\mathbf{z})$. Moreover, desingularization is necessary only when the target point \mathbf{z} is one of the vertices of the element over which integration is being performed. Suppose this is the case. Then we begin by writing the normal vector at a point \mathbf{x} on the element in terms of the normal vector at \mathbf{z} as

$$\mathbf{n}(\mathbf{x}) = \mathbf{n}(\mathbf{z}) + (\mathbf{x} - \mathbf{z}) \cdot (\nabla \mathbf{n})(\mathbf{z}) + \dots, \quad (44)$$

where, for the time being, we have assumed a sufficiently smooth representation of the surface for the sole of purpose of *deriving* a scheme for computing the singular part of the double layer integral. Now, the second term on the right hand side scales as δ_m/R , where $1/R$ is the local radius of curvature of the surface, while δ_m is the characteristic mesh size. For an undeformed capsule, $1/R = 1/a$, where a is the radius of the initial sphere. Therefore, a rough estimate of the second term on the right hand side is $O(\delta_m/a)$, which is expected to decay to zero linearly with δ_m under mesh refinement. Consequently, we assume the following

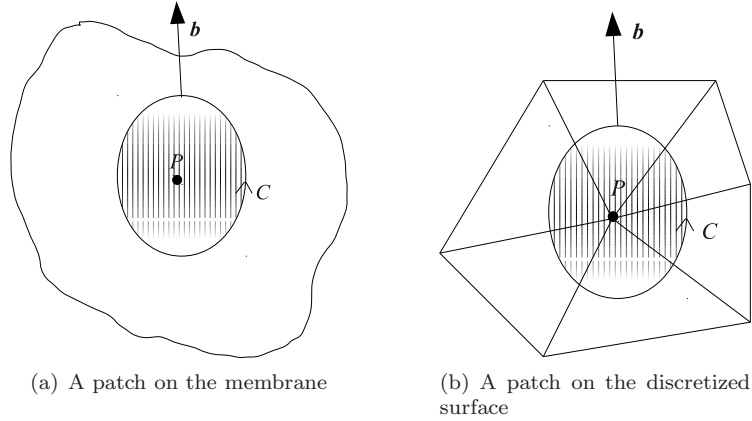


Figure 5: Defining the contour C enclosing an area (hatched) containing the point of interest P . \mathbf{b} is the in-plane normal to the contour C .

for the purposes of performing the singular double layer integral only

$$\mathbf{n}(\mathbf{z}) \approx \mathbf{n}(\mathbf{x}), \quad (45)$$

and therefore write the integral over the current element k as

$$[v_j^l(\mathbf{z})]_{S_k} = \int_{S_k} q_i(\mathbf{x}) T_{jik}^l(\mathbf{z}, \mathbf{x}) n_k(\mathbf{x}) dS(\mathbf{x}). \quad (46)$$

It is important to reemphasize that $\mathbf{n}(\mathbf{x})$ is now the normal vector of the triangle and not that of the vertex, as was the case in Eq. (42). If one substitutes the expression of \mathbf{T}^l from Eq. (12), one immediately sees that the singular parts of the integrand become identically zero as $\hat{x}_k n_k = \hat{\mathbf{x}} \cdot \mathbf{n} = 0$. This is due to the fact that elements are flat and $\hat{\mathbf{x}}$ lies in the plane of the element, while $\mathbf{n}(\mathbf{x})$ is normal to the element. This completes the evaluation of the local contribution to the double layer integral. The total double layer integral is then obtained as the sum of the local and the global parts as

$$v_j(\mathbf{z}) = v_j^l(\mathbf{z}) + v_j^g(\mathbf{z}). \quad (47)$$

3. Membrane Mechanics: Hydrodynamic traction jump

The solution of the boundary integral equation (3) requires the knowledge of the hydrodynamic traction jump across the interface $\Delta \mathbf{f}$. This jump in traction is obtained from the membrane equilibrium condition as discussed next. Consider first a patch of element on the membrane's surface as shown in Fig. (5a). The forces acting on this patch are the hydrodynamic stresses on the inner and the outer surface and the membrane tension at the boundary denoted by contour C . Now, let the membrane tension tensor be given

by $\boldsymbol{\tau}$, then the force balance on the membrane patch is given by

$$\int_{S_C} \Delta \mathbf{f} \, dS + \int_C \mathbf{b} \cdot \boldsymbol{\tau} \, dl = 0, \quad (48)$$

where S_C denotes the area enclosed by the contour C . Using the divergence theorem, one can convert to contour integral to a surface integral, which in the limit of infinitesimal area yields

$$\Delta \mathbf{f} = -\nabla_s \cdot \boldsymbol{\tau}, \quad (49)$$

where ∇_s is the surface divergence operator [1]. The above equation (49) has been directly employed in several boundary integral implementations to obtain the traction jump $\Delta \mathbf{f}$; see e.g. Lac et al. [23]. For flat elements as in this work, we note that $\boldsymbol{\tau}$ is constant over each element such that its surface divergence is identically zero, though there is a jump in its value across elements and consequently the contour integral in the Eq. (48) is generally expected to be non-zero. The Contour integral can therefore be used to obtain the traction jump as [39]

$$\Delta \mathbf{f} = -\frac{1}{A_C} \int_C \mathbf{b} \cdot \boldsymbol{\tau} \, dl, \quad (50)$$

where the A_C is the area enclosed by the contour C ; Fig. (5b) shows an example of the contour for the discretized surface. To proceed with our implementation, we first interpret the contour integral on the right of (50) as the reaction force on the given node, such that the strain energy stored in the membrane surface has been reassigned to the vertices of the discretized triangular elements. We then use the principal of virtual work as presented by Charrier et al. [5] to compute the reaction force at the vertices. Once the total reaction force \mathbf{F}_p at a given vertex P is known, we obtain the traction discontinuity at that vertex as

$$\Delta \mathbf{f}_p = -\frac{\mathbf{F}_p}{A_p} \quad (51)$$

where A_p is area assigned to the vertex, which is essentially the area enclosed by a hypothetical contour around the vertex P ; see Fig. (5b). We call the contour hypothetical as we never explicitly define it here. For the area assignment to the vertex, we use a very simple rule where each vertex of the triangular element is assigned a third of the triangular element's area. Therefore the total area A_p is obtained as (1/3) of the total area of the triangular elements of which the given vertex P is a member. We believe the method outlined here is substantially simpler to implement than employing the contour integral explicitly. In the remainder of this section, we outline the procedure employed for computing the reaction force at the vertices of the triangular elements.

We begin by introducing the formalism for describing the kinematics of the membrane deformation. This formalism is mostly clearly presented for deformations in a plane, which for the moment is taken to be the xy plane. Let (x, y) and (X, Y) denote respectively the undeformed and deformed coordinates of a material point, with respect to a fixed set of Cartesian axes. If u and v denote the displacements of the material

point in x and y directions respectively, then

$$\begin{aligned} X &= x + u, \\ Y &= y + v. \end{aligned} \tag{52}$$

The relationship between an infinitesimal line segment before and after the deformation can be expressed as

$$\begin{bmatrix} dX \\ dY \end{bmatrix} = \begin{bmatrix} 1 + \partial u / \partial x & \partial u / \partial y \\ \partial v / \partial x & 1 + \partial v / \partial y \end{bmatrix} \begin{bmatrix} dx \\ dy \end{bmatrix}, \tag{53}$$

or compactly as

$$d\mathbf{X} = \mathbf{F} \cdot d\mathbf{x}. \tag{54}$$

where \mathbf{F} is the deformation gradient tensor. The square of the distance between the two neighboring points after deformation is given by

$$\begin{aligned} dS^2 &= d\mathbf{X} \cdot d\mathbf{X} = d\mathbf{x} \cdot \mathbf{G} \cdot d\mathbf{x}, \\ \mathbf{G} &= \mathbf{F}^T \cdot \mathbf{F}, \end{aligned} \tag{55}$$

where \mathbf{G} is a symmetric positive definite matrix. We denote the eigenvalues of the \mathbf{G} by λ_1^2 and λ_2^2 , such that λ_1 and λ_2 are the principal stretch ratios. For a thin membrane that displays no resistance to bending, the strain energy density W of the membrane is a function of λ_1 and λ_2 . Here we consider the capsule to be an infinitely thin neo-Hookean membrane, for which the strain energy density is defined as [2]

$$W_{\text{NH}} = \frac{G}{2} \left[\lambda_1^2 + \lambda_2^2 + \frac{1}{\lambda_1^2 \lambda_2^2} - 3 \right]. \tag{56}$$

Here G is the two-dimensional shear modulus for the membrane, having units of force per unit length. To compute the reaction force at the nodes, we adopt the finite element approach of Charrier et al. [5]. Only the briefest account will be given here; for details the reader is referred to the original reference. In the approach of Charrier et al. [5], the membrane is discretized into flat triangular elements such that the strain is uniform over an element. Moreover, it is assumed that an element remains flat even after deformation. The forces at the nodes are then determined from the knowledge of the displacement of the vertices of the element with respect to the undeformed element followed by the application of the principle of virtual work, such that the computed forces and the known displacements are consistent with the strain energy stored in the element. For an arbitrarily oriented element, rigid body rotations and translations can be defined to make the deformed and undeformed state in the same plane. Note that the rigid body rotations and translations have no effect on the strain energy and consequently the forces. The forces are then computed using the coplanar formalism discussed above. Finally, these forces are transformed back to the frame of reference in the deformed state by applying the inverse transformation. The total reaction force at a node is obtained as a sum of reaction forces at that node due to contributions from all the triangular elements of which it is a member. Once the reaction force at any given node is known, the hydrodynamic traction

discontinuity at that node is obtained from Eq. (51) as detailed earlier.

4. Solution procedure and parameters

In this section we describe solution methods and parameters for the equations resulting from the formulation just presented.

The heart of the computation is the determination of the fluid velocity at the element nodes using equations (2) and (3). To compute the velocity from Eq. (2), we first need to compute the single layer density $\mathbf{q}(\mathbf{x})$. This is obtained from the solution of the integral equation (3). Upon discretization of the double layer integral in Eq. (3), which was discussed in Sec. (2.5), we obtain a linear coupled system of equations for \mathbf{q}^b , where \mathbf{q}^b is a vector of length $3N_b$ denoting the value of $\mathbf{q}(\mathbf{x})$ at the element nodes; N_b is the number of element nodes in the system. We express this linear system of equations as

$$(\mathbf{I} + \frac{\boldsymbol{\kappa}}{4\pi} \cdot \mathbf{D}^I) \cdot \mathbf{q}^b = \mathbf{b}, \quad (57)$$

where $\boldsymbol{\kappa}$ is a diagonal matrix of size $3N_b \times 3N_b$ denoting the value of κ_m in Eq. (3) at each element node, \mathbf{D}^I denotes the discretized double layer operator of size $3N_b \times 3N_b$, while \mathbf{b} is a $3N_b$ vector denoting the known right hand side of Eq. (3) at the element nodes. The above system of equations is solved iteratively using the GMRES algorithm [40]. An important benefit of this iterative procedure is that the matrix in the parenthesis above is never explicitly computed; at each iteration step only the product of the above matrix with a known vector generated by the algorithm is to be computed. The procedure to compute this matrix vector product is similar to computing $\mathbf{v}(\mathbf{z})$ in Sec. (2.5) (see Eq. 34) at the element nodes for a known \mathbf{q}^b . We take the initial guess for \mathbf{q}^b either from the previous time step, or from the previous stage if a multistage method is employed as is the case here. This leads to a substantial savings in the number of iterations required for convergence. Iterations were terminated when the L_2 norm of the current residual vector \mathbf{S} relative to the norm of the right hand side \mathbf{b} was less than 10^{-4} ; the residual vector \mathbf{S} is defined as

$$\mathbf{S} = (\mathbf{I} + \frac{\boldsymbol{\kappa}}{4\pi} \cdot \mathbf{D}^I) \cdot \mathbf{q}^b - \mathbf{b}. \quad (58)$$

In addition to the convergence in the residual vector \mathbf{S} , which is obtained naturally as part of the iterative procedure, it is also important to investigate the convergence in the solution; the error in solution denoted by vector \mathbf{S}_q is defined as

$$\mathbf{S}_q = \mathbf{q}^b - \mathbf{q}_{ex}^b \quad (59)$$

where we have defined the “exact” solution as \mathbf{q}_{ex}^b , which can be obtained by solving the above system of equations to a very small tolerance, e.g. 10^{-10} . The above tolerance of 10^{-4} for the residual vector relative to the norm of the right hand side leads to an error of the same order for the error vector relative to the exact solution for well conditioned systems. This implies an accuracy of 0.01% for most cases. Even for the worst

case discussed later, the relative error in the solution was less than 0.1%. In most cases convergence was achieved in less than 5 iterations; see Sec. (6) for some examples. For systems with high viscosity contrast and/or with large number of particles, the matrix may become ill-conditioned and a preconditioner may become necessary. In the present study, no preconditioner was employed, though multigrid preconditioners for Stokes flow may be useful [41, 9].

The iterative procedure described above gives the \mathbf{q}^b vector at the element nodes. These are subsequently substituted in Eq. (2) to compute the corresponding velocity at the element nodes; the numerical procedure described in Sec. (2.4) is employed to compute this single layer integral. We denote the velocity thus computed at the element nodes by a $3N_b$ vector \mathbf{u}^b , which is used to evolve the position of element nodes \mathbf{x}^b as per the equation

$$\frac{d\mathbf{x}^b}{dt} = \mathbf{u}^b. \quad (60)$$

The time integration in the above equation is performed via the second order midpoint method, which belongs to the family of explicit Runge-Kutta integrators [25]. The time step Δt employed in this work was set adaptively using the rule $\dot{\gamma}\Delta t = 1/2 Ca \Delta x_{min}/a$ [38, 29], where Δx_{min} is the minimum node-to-node separation in the system (which does not have to be for two points on the same particle), a quantifies the length scale of the particle such as the radius for a spherical particle, $\dot{\gamma}$ is the shear rate, while Ca is the capillary number, expressing the ratio of viscous and interfacial stresses (for a spherical capsule with radius a and shear modulus G , the capillary number is defined as $Ca = \mu\dot{\gamma}a/G$). This rule gave a stable evolution with time; a time step twice this value led to an instability in some simulations presented later, while a time step half this size gave nearly indistinguishable result. The volume of the particle was found to be well conserved with time. For example, for a capsule with $\lambda = 5$ in shear flow at $Ca = 0.6$, the volume changed by an average of 10^{-4} of its original value over a unit strain. In the present work, a volume correction was performed only when the volume of the particle deviated by more than 10^{-4} of its original value; the procedure employed for this correction is described in Freund [10].

Finally, we consider parameters related to the numerical solution procedure. Many of these have already been introduced earlier, and are repeated here for completeness. The first parameter is N_Δ , which refers to the number of triangular elements employed to discretize the surface of each of the N_p particles in the system; the number of element nodes per particle is denoted by N_b . Next, there are several parameters associated with the GGEM methodology described in Sec. (2.2). First is the length scale α^{-1} associated with the quasi-Gaussian global density. The solution of the global problem in Sec. (2.2) requires one to define a three dimensional mesh with N_x , N_y , and N_z mesh points in x , y and z directions respectively. This gives a mean mesh spacing in the three directions as $\Delta x_m = L_x/N_x$, $\Delta y_m = H/(N_y - 1)$ and $\Delta z_m = L_z/N_z$; all three mean mesh spacings are kept equal unless otherwise mentioned. An important parameter denoting the resolution of the GGEM methodology is $\alpha\Delta y_m$, with the resolution and hence the accuracy of the

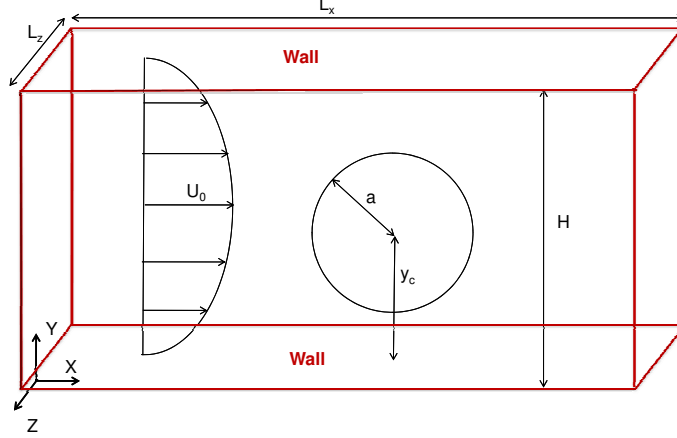


Figure 6: Schematic of the slit geometry for the test problems in Secs. (5.1) and (5.2). A single sphere, either a rigid particle or a drop, is placed in a slit geometry with the channel height being H . The radius of the sphere is a , while its center is at y_c . A pressure driven flow is considered with U_0 being the centerline velocity. The confinement ratio is $2a/H$. Periodic boundary conditions are employed in \mathbf{x} and \mathbf{z} directions, with periodicity being L_x and L_z respectively.

method increasing with decreasing $\alpha\Delta y_m$. As a rule of thumb, we require $\alpha\Delta y_m < 1$; see Sec. (2.2) for details. Choices of above parameters are specified below in the descriptions of the test problems.

5. Numerical Results: Validation

5.1. Single layer validation: Rigid particle in a slit

As a validation of the single layer integral implementation, we consider a rigid sphere between two parallel walls and subject it to a pressure driven flow with a centerline velocity U_0 as shown in Fig. (6). For a rigid particle, the velocity at a point \mathbf{x}_0 on the surface satisfies the following integral equation [21]

$$u_j(\mathbf{x}_0) = u_j^\infty(\mathbf{x}_0) - \frac{1}{8\pi\mu} \int_S f_i(\mathbf{x}) G_{ji}(\mathbf{x}_0, \mathbf{x}) dS(\mathbf{x}), \quad (61)$$

where \mathbf{f} is the traction on the external surface of the sphere due to the stresses in the fluid. The velocity at the surface of the particle $\mathbf{u}(\mathbf{x}_0)$ in the above equation can be written as

$$\mathbf{u}(\mathbf{x}_0) = \mathbf{U} + \mathbf{\Omega} \times (\mathbf{x}_0 - \mathbf{x}_c), \quad (62)$$

where \mathbf{U} and $\mathbf{\Omega}$ represent the translational and rotational velocities of the particle, and \mathbf{x}_c denotes the center of the sphere. Here we take the particle to be force and torque free and our goal is to compute the velocity and angular velocity of the particle. For this particular problem, the surface of the sphere was discretized into $N_\Delta = 5120$ triangular elements with $N_b = 2562$ vertices. The unknowns in the discretized system are $3N_b$ tractions at element vertices, along with \mathbf{U} and $\mathbf{\Omega}$. The force and torque free condition along with the discretization of Eq. (61) gives $3N_b + 6$ equations, which were solved iteratively using the GMRES algorithm [40].

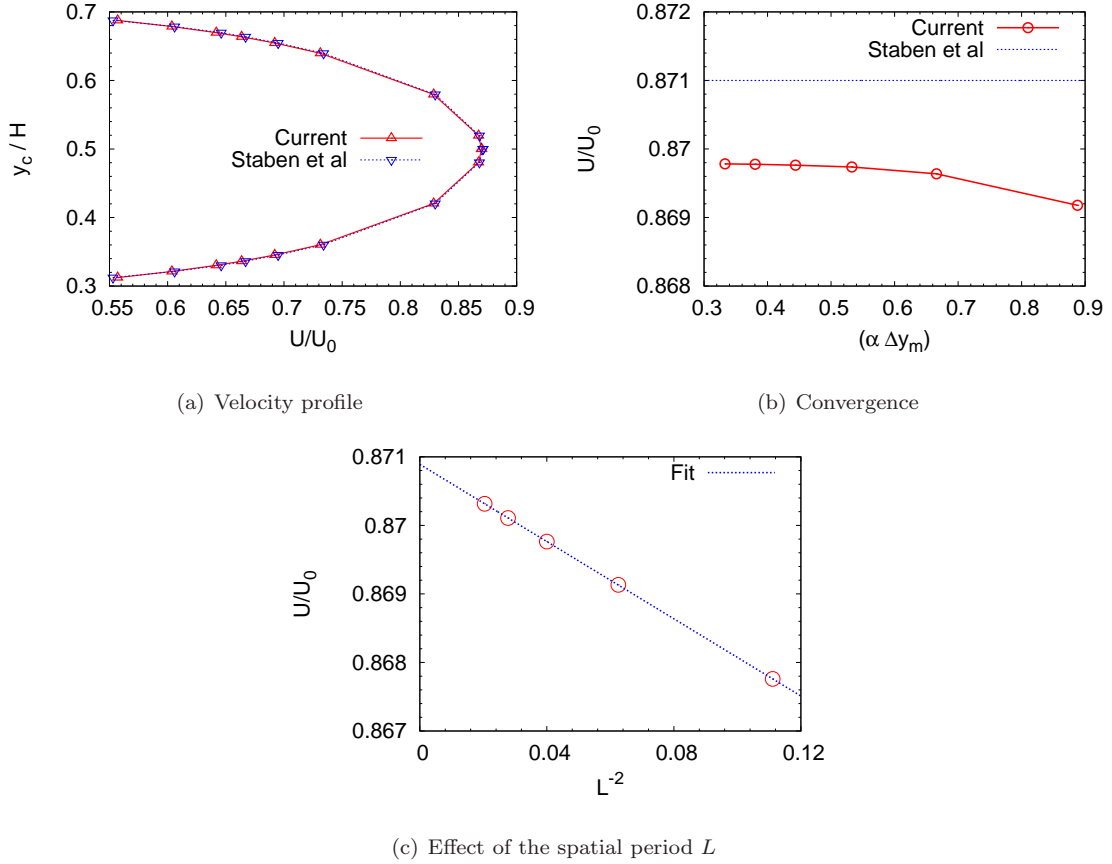


Figure 7: Rigid particle in a slit: (a) Comparison of the translational velocity of a rigid sphere in a slit geometry with results of Staben et al. [42]. The confinement ratio of the particle was $2a/H = 0.6$. The horizontal axis gives the velocity of the particle non-dimensionalized by the centerline velocity of the undisturbed fluid, while the vertical axis gives the location of the center of the sphere along the gradient direction non-dimensionalized by the height of the channel. Walls are present at $y = 0$ and $y = H$. Simulation parameters were: $N_y = 61$, $\alpha\Delta y_m = 0.44$, $N_\Delta = 5120$, $L_x = L_z = 5H$, and $\Delta x_m = \Delta y_m = \Delta z_m$; see text for details. (b) Convergence of the velocity for $y_c/H = 0.5$ with $\alpha\Delta y_m$. For this calculation $r_{cut} = 0.5a$ is kept fixed, while N_y is varied between 17 and 81. (c) Effect of the spatial period $L = L_x = L_z$ on the translational velocity of a particle with $y_c/H = 0.5$. Also shown is a linear fit to the data in the plot. All simulation parameters in (c) were the same as in (a) above except for L_x and L_z which were varied.

Translational and rotational velocities of a rigid sphere between two infinite parallel walls have been reported previously by Staben et al. [42]. Here, we compare the translational velocity obtained in the present work with their results for a fixed confinement ratio of $2a/H = 0.6$ and for various positions of the sphere's center along the channel height y_c . This comparison is shown in Fig. (7a), where the velocity of the particle has been non-dimensionalized by the velocity of the undisturbed flow at the centerline U_0 , while the height of the sphere's center has been non-dimensionalized by the channel height H . Very good agreement between the two results was observed, with the discrepancy typically being less than 0.8%; possible sources for the slight discrepancy are discussed below. The GGEM parameters employed for this calculation were: $N_y = 61$ and $r_{cut} = 0.5a$, which gives $\alpha\Delta y_m = 0.44$; note that $r_{cut} = 4/\alpha$. The mean mesh spacing was equal in all three directions ($\Delta x_m = \Delta y_m = \Delta z_m$), and the spatial period in both x and z directions were

set to five times the wall spacing: $L_x = L_z = 5H$. The convergence of the particle's velocity with respect to $\alpha\Delta y_m$ is demonstrated next in Fig. (7b), where the particle was placed at the centerline, i.e. $y_c/H = 0.5$. For this calculation $r_{cut} = 0.5a$ was held constant, while $\alpha\Delta y_m$ was varied by varying N_y between 17 and 81 (N_x and N_z varied between 80 and 340). As could be seen in the figure, the velocity of particle reaches its converged value for $\alpha\Delta y_m < 0.5$ and shows very little variation with any further increase in mesh resolution. Also shown in this plot is the result of Staben et al. [42] which reveals that the velocity obtained in this work converges to a slightly lower value than the previous reference. The source of this discrepancy can be traced to the periodic boundary conditions employed in x and z directions in the present work; Staben et al. [42] used an unbounded domain in these directions. This notwithstanding, we can estimate the result for an infinite box by observing the trends in a series of simulations with varying spatial period L ($L = L_x = L_z$). This procedure is commonly used in triply periodic simulations to remove the effects of the periodic boundary conditions; see, e.g. [22]. This procedure usually requires the knowledge of the scaling of the periodic image effects with the spatial period L . The particle considered here is force and torque free, and hence to leading order is a stresslet – a symmetric force dipole. An analytical expression for the velocity due to a point force in a slit with periodic boundary conditions in x and z directions is available [27], though the scaling of the periodic image effects with the spatial period L is not immediately obvious. At this point it may be interesting to note that the velocity parallel to the walls due to a point force parallel to the walls in an infinite slit is known to decay as r^{-2} at large distance r from the point force [28]; the velocity due to a force-dipole is therefore expected to decay as r^{-3} . Though the scaling of the periodic image effects in our case is not obvious, we numerically find that these effects decay as L^{-2} as shown in Fig. (7c), where we have plotted the translational velocity of the particle against L^{-2} . The y-intercept of the linear fit through the data points in the previous plot then gives the estimate for the particle's velocity in an infinite slit. This value comes out to be $0.871U_0$ (rounded to three significant digits), which is exactly equal to the value reported by Staben et al. [42]. In addition to the periodic image effects, a slight discrepancy between the two results can also be expected in cases where the particle-wall separation is very small. In such problems, a large lubrication pressure can develop in the region around the small gap [21]. To obtain accurate solutions in this case, the surface discretization of the particle near the small gap must be adaptively refined as was done by Staben et al. [42]. No fundamental changes to the present formalism would be required to implement adaptive refinement.

5.2. Single and double layer validation: A Drop in a slit

Having validated the single layer integral, we next move on to the validation of the double layer integral. For this, we consider the same geometry and bulk flow as in the above test case (Fig. 6), but now consider a spherical drop instead of a rigid sphere. The motion of the drop can be obtained by first solving Eq. (3) for $\mathbf{q}(\mathbf{x})$, which upon substitution in Eq. (2) gives the velocity on the surface of the drop. We first point out

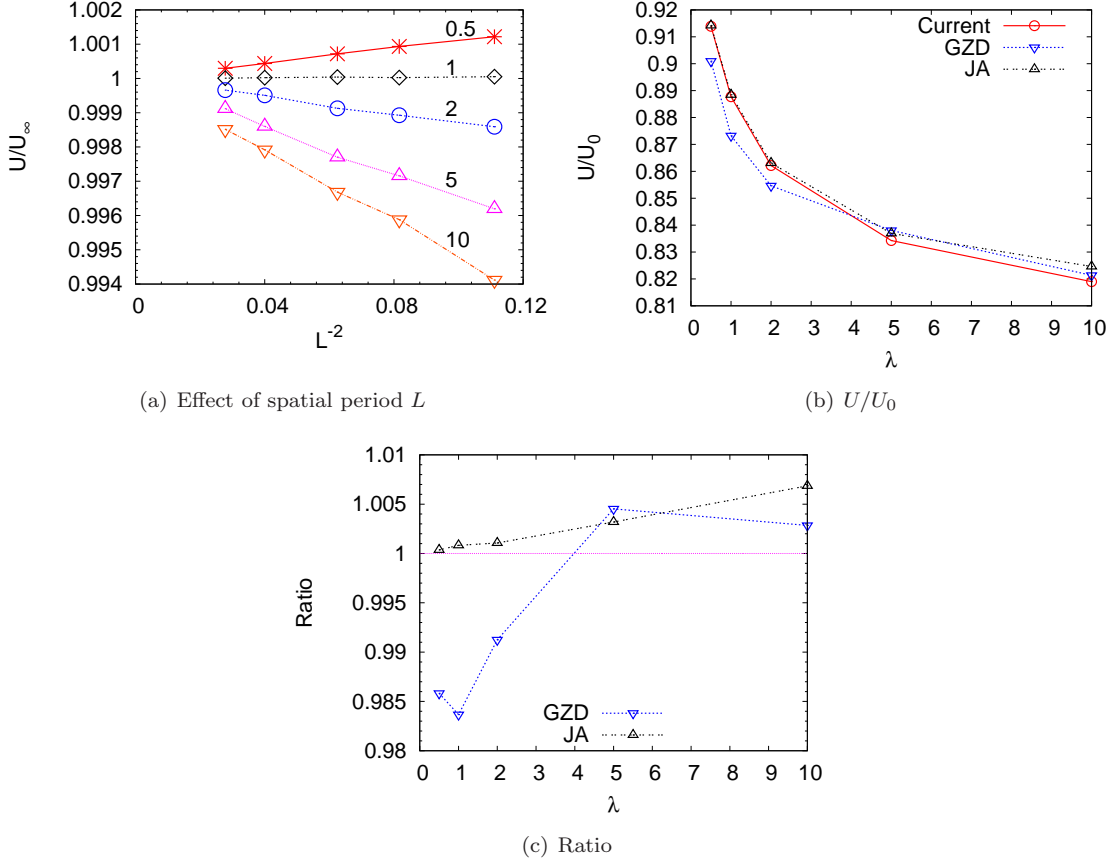


Figure 8: Volume averaged translational velocity of a spherical drop in a slit. The confinement ratio of the drop is $2a/H = 0.6$, while its center is at $y_c/H = 0.4$. The simulation parameters are: $N_y = 61$, $\alpha\Delta y_m = 0.44$, $N_\Delta = 5120$, and $\Delta x_m = \Delta y_m = \Delta z_m$. (a) Effect of the spatial period $L = L_x = L_z$ on the drop's velocity for different viscosity ratio λ . Note the velocity has been non-dimensionalized by U_∞ , which is the estimated velocity of the drop as $L_x \rightarrow \infty$ and $L_z \rightarrow \infty$. This is obtained by fitting a straight line to the data which have not been non-dimensionalized by U_∞ ; the y-intercept of this fit gives U_∞ . (b) Comparison of the volume averaged translational velocity of the drop as a function of viscosity ratio in a slit geometry with results of Griggs et al. [14] (GZD) and Janssen and Anderson [20] (JA). Data from the two references have been read off at $t = 0$, i.e. they correspond to the velocity of an initially spherical drop. Note that there was some degree of uncertainty in reading off the data from the figures at $t = 0$. The velocity in the current work corresponds to U_∞ in (a) above. (c) Literature values in (b) plotted as a ratio with the results of the present work. Notice the small range of ordinate in the plot.

that for a spherical drop, the interfacial traction jump $\Delta \mathbf{f}$ is inconsequential. This is due to the fact that $\Delta \mathbf{f}$ is uniform in strength and acts radially everywhere, which when combined with the incompressibility of the fluid implies zero velocity contribution from this term. Once the velocity at the surface of the drop is known, we compute the volume averaged velocity of the drop as

$$U_i = \frac{1}{V} \int_V u_i dV = \frac{1}{V} \int_S (u_j n_j) x_i dS, \quad (63)$$

where V represents the volume of the drop, while \mathbf{n} is the unit normal vector at the surface. We computed the instantaneous volume averaged velocity of a spherical drop placed at $y_c/H = 0.4$ and with a confinement ratio of $2a/H = 0.6$ for different drop viscosity ratios λ . The simulation parameters for this calculation were kept

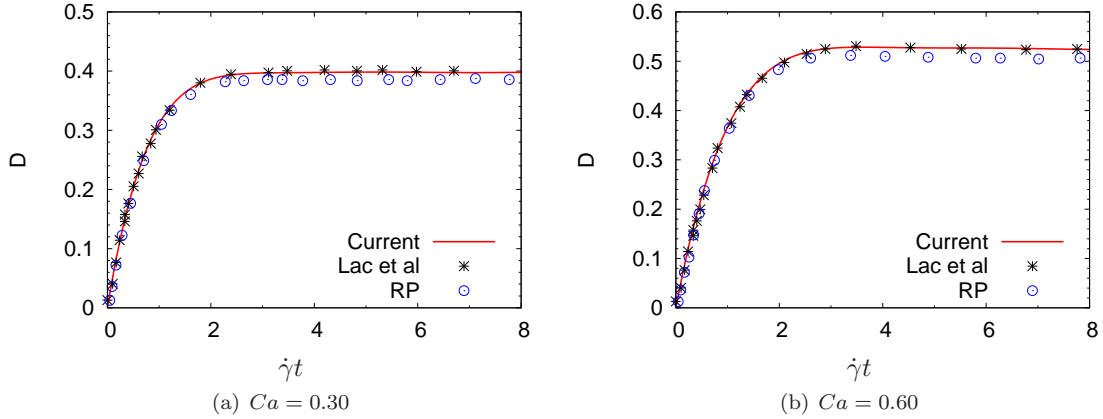


Figure 9: $\lambda = 1$: Time evolution of the Taylor deformation parameter. Lac et al in the plot refers to results of Lac et al. [23], while RP refers to results of Ramanujan and Pozrikidis [39]. Simulation parameters were: $L_x = L_y = H = 15a$, $N_y = 97$, $r_{cut} = a$, $\alpha\Delta y_m = 0.625$, $N_\Delta = 5120$, and $\Delta x_m = \Delta y_m = \Delta z_m$.

the same as in the previous section, namely $N_y = 61$, $N_\Delta = 5120$, $\alpha\Delta y_m = 0.44$, and $\Delta x_m = \Delta y_m = \Delta z_m$. Just like in the case of rigid particle above, we again find the same L^{-2} scaling of the periodic image effects on the drop velocity. This is shown in Fig. (8a) for drops of different viscosity ratios λ , where the velocity of the drop has been non-dimensionalized by the corresponding velocity estimated for an infinite slit using the procedure outlined above in Sec. (5.1). Interestingly, for a drop with $\lambda = 1$, there is no observable periodicity effect, while the drop velocity increases with increasing L for $\lambda > 1$ and decreases with increasing L for $\lambda < 1$.

In Fig. (8b), we compare the results in the present work corrected for periodicity effects with those of Griggs et al. [14] and Janssen and Anderson [20] for several viscosity ratios ($\lambda \in [0.5, 1, 2, 5, 10]$). For a better comparison, we also plot the ratio of velocity obtained from previous references and the present work in Fig (8c). A very good agreement between our results and that reported by Janssen and Anderson [20] is obtained at all viscosity ratios (error $< 0.7\%$), though the discrepancy between the two results monotonically increases with increasing λ . The cause for this behavior is not clear. The agreement with the results of Griggs et al. [14] is equally good or better at higher viscosity ratios ($\lambda \geq 5$) with no obvious dependence of the discrepancy on λ at high λ . The discrepancy with the previous work at low viscosity ratios is most likely associated with errors in reading the data from their plot, since for matched viscosity problems ($\lambda = 1$), the velocity throughout the domain is the same as the undisturbed velocity. In such a case, the volume averaged velocity of the drop can be computed analytically, which yields: $U = 0.888 U_0$; this value agrees with the result of the present work.

5.3. Validation of the capsule membrane mechanics and the overall implementation

We next consider a capsule in a simple shear flow. To enable comparison with literature results in an unbounded domain, we consider a large simulation box with $L_x = H = L_z = 15a$, where a is the radius of

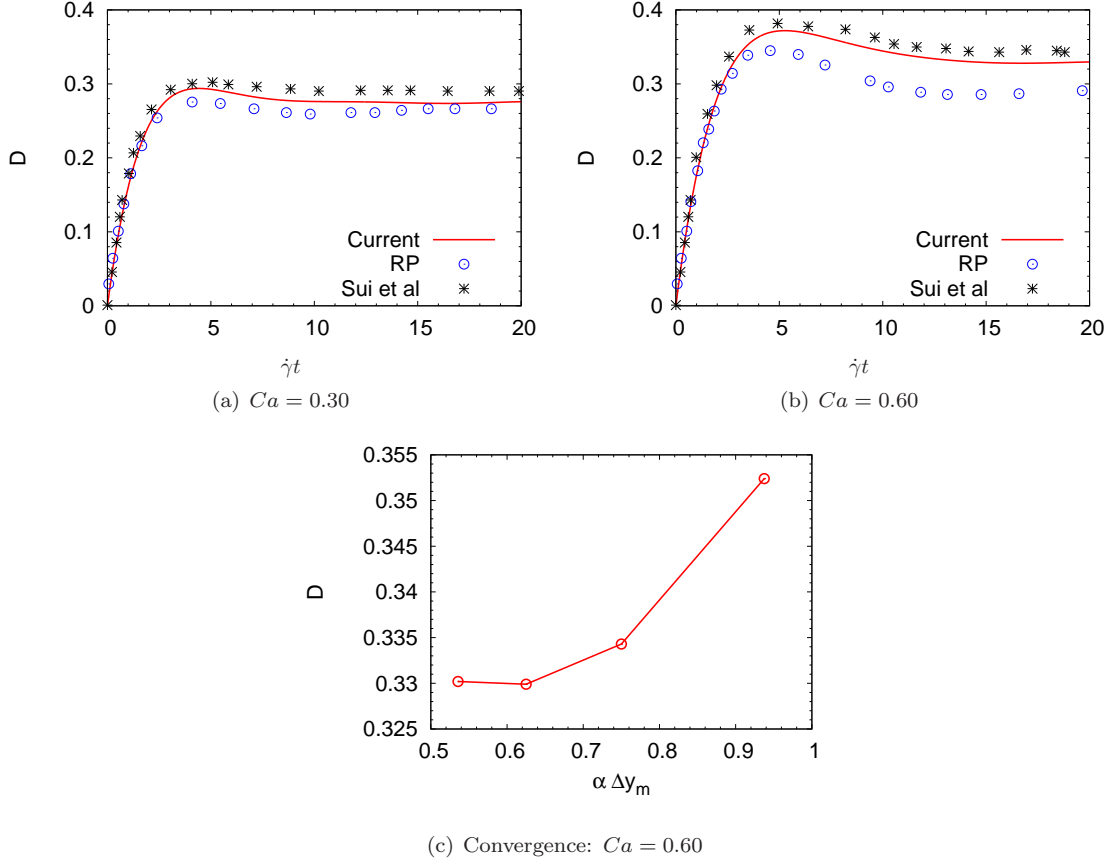


Figure 10: $\lambda = 5$: (a) & (b) Time evolution of the Taylor deformation parameter. Results from the current study are compared with the work of Sui et al. [44] and Ramanujan and Pozrikidis [39] (RP). Simulation parameters were the same as in Fig. (9). (c) Convergence of D with $\alpha\Delta y_m$ at $Ca = 0.6$. Data points in the plot is obtained by varying N_y while holding $r_{cut} = a$ fixed.

the initially spherical capsule placed at the center of the box. Other simulation parameters were: $N_y = 97$, $r_{cut} = 1.0$, $\alpha\Delta y_m = 0.625$, $N_\Delta = 5120$, and $\Delta x_m = \Delta y_m = \Delta z_m$; a convergence study with these parameters will be presented for $\lambda = 5$ capsule later in this section. The system is subjected to simple shear flow and we follow the evolution of the shape of capsule at various capillary numbers ($Ca = \mu\dot{\gamma}a/G$) and viscosity ratios (λ). Lac et al. [23] showed that a membrane lacking bending resistance buckles at high or low Ca ; the origin of this buckling has been shown to be numerical [26]. We saw a similar behavior here and therefore restrict the results reported here to $0.3 \leq Ca \leq 0.6$. In this regime, the capsule membrane evolution appeared to be stable with no apparent buckling. To characterize the shape of the deformed capsule, we introduce the commonly employed Taylor deformation parameter D , which is defined as

$$D = \frac{L - B}{L + B}, \quad (64)$$

where L and B are the maximum and the minimum distance in the shear plane of a point on the surface of the capsule from its center. We use this as the definition of D , though some authors, e.g. Ramanujan and

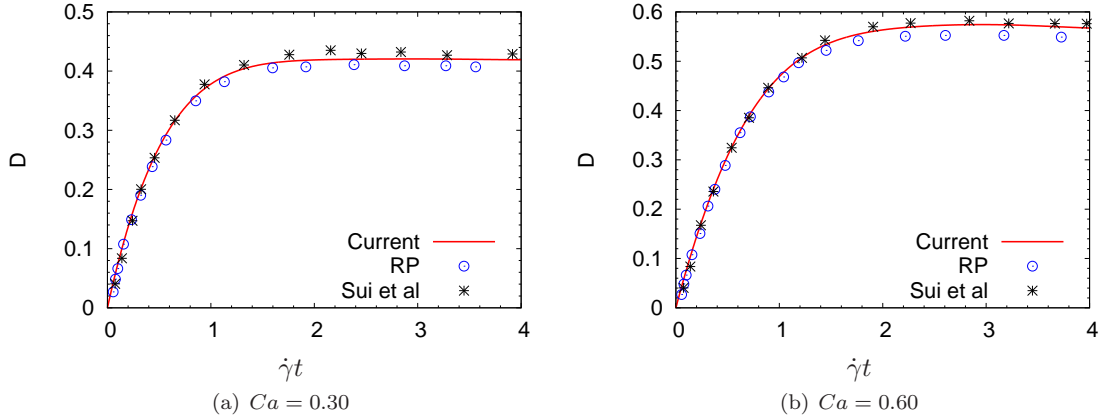


Figure 11: $\lambda = 0.2$: Time evolution of the Taylor deformation parameter. Results from the current study are compared with the work of Sui et al. [44] and Ramanujan and Pozrikidis [39] (RP). Simulation parameters were the same as in Fig. (9)

Pozrikidis [39], instead find a triaxial ellipsoid with the same inertia tensor as the given capsule, and then take L and B as the major and minor axis of that ellipsoid.

The evolution of the deformation parameter D for a capsule with unit viscosity ratio ($\lambda = 1$) is shown in Fig. (9) for three different capillary numbers Ca . The time in the figures has been non-dimensionalized by the shear rate. For comparison, D values reported by Ramanujan and Pozrikidis [39] and Lac et al. [23] are also plotted. Note that Ramanujan and Pozrikidis [39] have used a zero-thickness shell model for their capsules, though that gives only marginally lower deformation than a neo-Hookean capsule at the same Ca [39]. Moreover, they used the Young's modulus for computing their Ca , such that our results should be compared with their results at a Ca which is $(1/3)$ of the Ca in this work. The data in Fig. (9) at various Ca shows that the evolution of D in this work is in very good agreement with the corresponding results of Lac et al. [23]. Our results are also close to the values reported by Ramanujan and Pozrikidis [39], though the latter consistently display a slightly lower D . The broad agreement of D between our values and the literature values validates our implementation of the membrane mechanics along with other aspects of our method such as time-stepping and the already validated single layer integral.

We next briefly discuss the deformation parameter results for capsules with non-unit viscosity ratios (i.e. $\lambda \neq 1$). These are reported in Fig. (10) for $\lambda = 5$ and in Fig. (11) for $\lambda = 0.2$, and are compared with the results of Ramanujan and Pozrikidis [39] and Sui et al. [44], with the latter reference employing the lattice-Boltzmann technique for their simulations. At $\lambda = 5$, the results for D in the present work are slightly smaller than that reported by Sui et al. [44]. This could be due to the different fluid flow solver employed by Sui et al. [44]. The D computed in the present effort is slightly larger than the results of Ramanujan and Pozrikidis [39] at $Ca = 0.3$, though the discrepancy is substantial at $Ca = 0.6$. The source of this discrepancy is not clear. For $\lambda = 0.2$ (Fig. 11), good agreement with the results of Ramanujan and Pozrikidis [39] and Sui et al. [44] was observed, though values reported by Sui et al. [44] are marginally

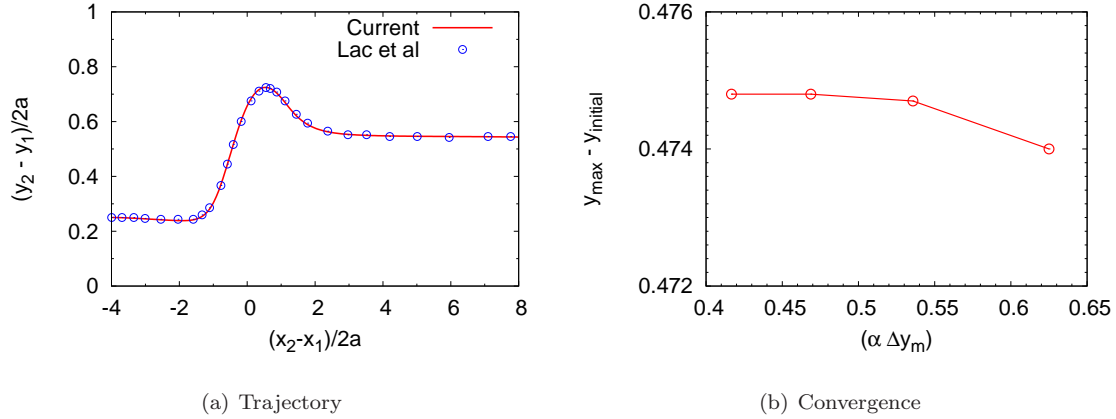


Figure 12: Pair collision: $\lambda = 1$. (a) Shows the separation between the center of masses of capsules in the gradient direction as a function of their separation in the flow direction. Also plotted is the corresponding result from Lac et al. [24]. Simulation parameters were: $L_x = L_y = H = 30a$, $N_y = 129$, $r_{cut} = 2a$, $\alpha\Delta y_m = 0.0469$, $N_\Delta = 1280$, and $\Delta x_m = \Delta y_m = \Delta z_m$. (b) Convergence of the maximum displacement of either particle (absolute value) from its initial position along the gradient direction (y) as a function of $\alpha\Delta y_m$. Data points in this curve were obtained by holding $r_{cut} = 2a$ fixed and varying N_y .

higher, while those reported by Ramanujan and Pozrikidis [39] are marginally lower. Lastly, we show the convergence of steady state D with the GGEM parameter $\alpha\Delta y_m$. For this calculation, $r_{cut} = a$ was held fixed, while N_y was varied between 65 and 113. As could be seen, a convergence in D is observed at $N_y = 97$ corresponding to $\alpha\Delta y_m = 0.625$ – the parameter set for which all results were reported in this section.

5.4. Pair collision

As a final test problem, we consider the collision between a pair of capsules with $\lambda = 1$ in a simple shear flow and compare the results with the work of Lac et al. [24] in Fig. (12a). We first describe the problem setup. The size of the cubic box (slit) for this problem was set to $30a$ to approximate an unbounded domain; simulations were performed with $N_y = 129$, $r_{cut} = 2a$, $\alpha\Delta y_m = 0.469$, $N_\Delta = 1280$, and $\Delta x_m = \Delta y_m = \Delta z_m$. The two capsules were initially kept in the same flow-gradient plane ($x - y$), such that the initial separation in the flow direction was $x_2 - x_1 = -8a$, while the initial offset in the gradient direction was $y_2 - y_1 = 0.5a$. As in Lac et al. [24], we preinflate the capsule by 5%, i.e. the radius of the spherical capsule was increased by 5% over its rest value, and this new increased radius is denoted by a . For a spherical shape, this inflation does not lead to any flow due to the incompressibility condition as discussed above in the case of a spherical drop. Nonetheless, this inflation keeps the membrane in a state of tension at rest and if sufficient will prevent buckling during the course of collision. With these preliminaries, we return to Fig. (12a) where we show the relative separation between the center of masses in the gradient direction and the corresponding separation in the flow direction. Again, very good agreement is observed. Lastly, we show the convergence of the numerical scheme with $\alpha\Delta y_m$ in Fig. (12b), where we plot the absolute value of the maximum displacement in the gradient direction for either particle. For this calculation $r_{cut} = 2a$ was held fixed, while N_y was varied between 97 and 145. A convergence is seen at $\alpha\Delta y_m = 0.469$ corresponding to $N_y = 129$ – the

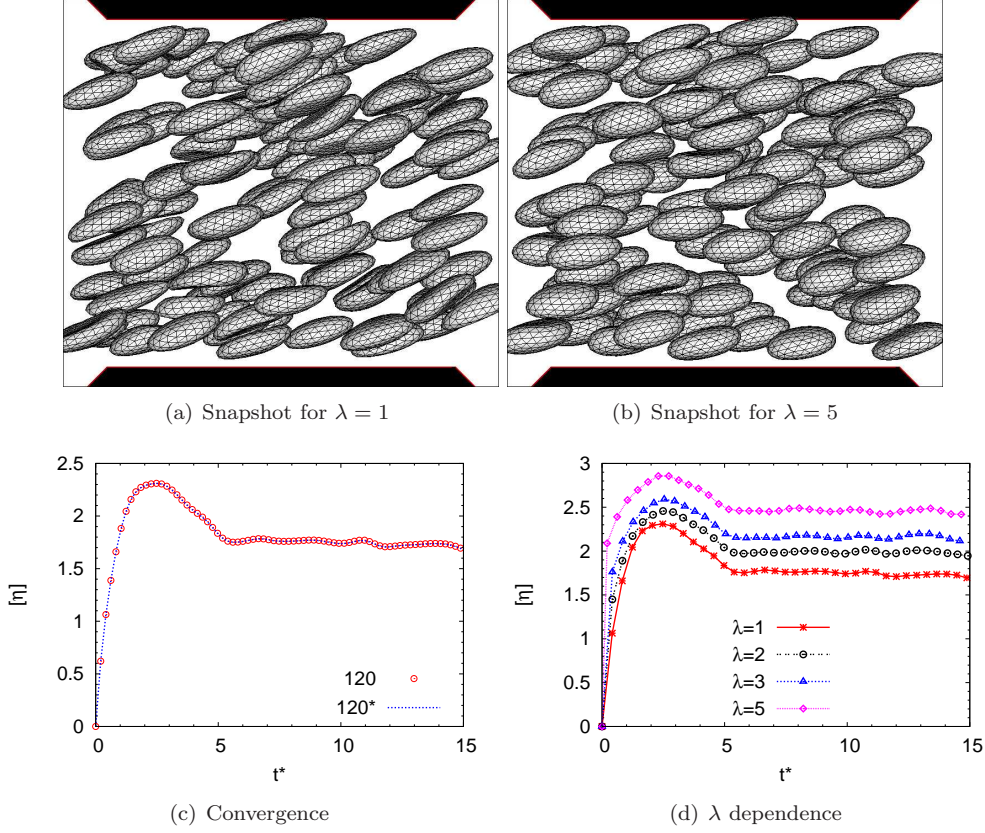


Figure 13: Apparent intrinsic viscosity $[\eta]$ for sheared suspensions of capsules with $Ca = 0.5$ and volume fraction $\phi = 0.15$. (a) Snapshot for $\lambda = 1$ capsule with $N_p = 120$, (b) Snapshot for $\lambda = 5$ capsule with $N_p = 120$, (c) Convergence in viscosity for $\lambda = 1$ capsules with $N_p = 120$ particle system. The simulation parameter $\alpha\Delta y_m$ was 0.5 for the run labeled 120, while it was 0.417 for the run labeled 120*, (d) Effect of λ on the apparent intrinsic viscosity for $N_p = 120$ particle system. The simulation parameters in all cases above were: $r_{cut} = a$, $\alpha\Delta y_m = 0.5$, $N_\Delta = 320$, and $\Delta x_m = \Delta y_m = \Delta z_m$ unless otherwise mentioned.

parameters for which results are reported in Fig. (12a).

6. Multiparticle Simulations: suspension viscosity and computational complexity

In this section, we report results from several large scale simulations on multiparticle suspensions of capsules. In the first part of the section, we present results for the suspension viscosity and discuss its dependence on the viscosity ratio. In the second part, we discuss the expected computational complexity of the algorithm and verify it with the timing results from the multiparticle simulations.

6.1. Suspension viscosity

We consider here a suspension of Neo-Hookean capsules in a cubic slit (Fig. 13a,b). These suspensions are subjected to a simple shear flow at a capillary number of $Ca = 0.5$; the volume fraction of the suspension is $\phi = 0.15$, which is typical of the blood flow in the microcirculation [11]. Capsules with four different viscosity ratios λ are considered: $\lambda = 1$, $\lambda = 2$, $\lambda = 3$ and $\lambda = 5$. The surface of each of the capsules in this

study was discretized into $N_\Delta = 320$ triangular elements, while four different system sizes were considered with the number of particles being $N_p = 15$, $N_p = 30$, $N_p = 60$, and $N_p = 120$. The number of degrees of freedom in these four systems are 7290, 14580, 29160, and 58320 respectively. In each of the problems, $r_{cut} = a$ was kept fixed, where a is radius of the spherical capsule at rest. Similar to Sec. (5.4), the capsules were preinflated by 5% to prevent membrane buckling; the radius after preinflation is denoted by a . The number of mesh points N_y for the global solution varied between 61 and 121 such that $\alpha\Delta y_m = 0.5$ along with $\Delta x_m = \Delta z_m = \Delta y_m$. For testing the convergence of the results with respect to GGEM parameters, some simulations were also run with 20% extra mesh points in each of the directions corresponding to $\alpha\Delta y_m = 0.417$. The simulations were initiated by placing the particles randomly in the simulation box, and then they were sheared for a total non-dimensional time of $t^* = \dot{\gamma}t = 15$. We show some representative snapshots from the simulations at $t^* = 15$ and $N_p = 120$ in Fig. (13a) for $\lambda = 1$ capsules and in Fig. (13b) for $\lambda = 5$ capsules. It is immediately obvious from these snapshots that the more viscous capsules deform less and also have a smaller inclination angle with the flow direction; both of these observations are similar to observations in isolated sheared capsules [39]. We next demonstrate the convergence of the simulation with respect to GGEM parameters by plotting the suspension apparent intrinsic viscosity $[\eta]$ for $\lambda = 1$ capsule and $N_p = 120$ particles for two different mesh resolutions corresponding to $\alpha\Delta y_m = 0.5$ and $\alpha\Delta y_m = 0.417$ in Fig. (13c). The apparent intrinsic viscosity is defined as $[\eta] = \Sigma_{xy}^p / (\mu\phi\dot{\gamma})$, where Σ_{xy}^p is the particle contribution to shear stress, while μ is the suspending fluid viscosity. The particle contribution to the stress tensor is given by

$$\Sigma_{ij}^p = \frac{1}{V} \sum_{m=1}^{N_p} \int_{S_m} [\Delta f_i x_j + \mu(\lambda - 1)(u_i n_j + u_j n_i)] dS, \quad (65)$$

where the sum in the right hand side is over all the particles in the system. As can be seen in Fig. (13c), $[\eta]$ is nearly identical for simulations run with $\alpha\Delta y_m = 0.5$ and $\alpha\Delta y_m = 0.417$, thereby demonstrating the convergence of the simulation with respect to GGEM parameters. All the remaining simulations were performed with $\alpha\Delta y_m = 0.5$. The effect of viscosity ratio on the apparent intrinsic viscosity is presented in Fig. (13d); these results have been obtained from a $N_p = 120$ particle system. We find in the figure that $[\eta]$ increases with increasing λ . It may also be interesting to note that the steady state $[\eta]$ in all cases is less than 2.5, which is the expected value of $[\eta]$ for suspensions of rigid spheres at infinite dilution.

6.2. Computational complexity

We devote the remainder of this section to analyzing the overall computational complexity of our algorithm. Before presenting the timing results from the detailed numerical simulations presented above, it will be useful to first discuss the expected computational cost associated with various steps in the algorithm, and consequently the overall implementation. The first step in the solution procedure, as discussed in Sec. (4), involves iteratively solving for the single layer density \mathbf{q}^b (step 1). This is followed by the computation of

the fluid velocity \mathbf{u}^b at the element nodes (step 2) using the single layer density \mathbf{q}^b computed in the previous step. The computational cost associated with each iteration of step 1 and that of step 2 has an identical optimal scaling with $N = N_\Delta \times N_p$, each of which is essentially determined by the computational cost associated with the Stokes flow solver (GGEM) described in Sec (2.2). Therefore, for a direct cost comparison with the multiparticle flow problem here, we consider an auxiliary problem involving a collection of N point forces; both problems then have an identical computational cost scaling with N .

The overall cost associated with the Stokes flow solver is the sum of costs associated with the local problem and the global problem. The cost of the local solution scales as the product of the number of point forces N and the number of neighbors within a distance $r_{cut} \sim \alpha^{-1}$ of each of the point forces. If we require the computational cost of the local problem to scale as $t_l \sim O(N)$, then the number of neighbors per point force must stay constant with changing system size (meaning N here). The system size N can be increased in two contrasting ways: (i) at constant density and increasing volume (i.e. N/V is constant, V is the system volume), and (ii) at constant volume and increasing density. If the system size is increased at constant density, we require that α (or r_{cut}) be held constant, and if the system size is increased at constant volume, we require that $\alpha \sim N^{1/3}$ (or $r_{cut} \sim N^{-1/3}$). This scheme for choosing α ensures that the average number of near neighbors per point force is independent of the system size. Hence, irrespective of how N is varied, we always obtain $t_l \sim O(N)$. Next, we determine the computational cost of the global solution procedure. Before we proceed further, it is important to realize that the error in the global solution is essentially controlled by the parameter $\alpha\Delta y_m$; see Sec. (2.2.2). Therefore, for the error in the global solution to remain of the same order with changing system size N , we require that $\alpha\Delta y_m$ be held constant; this implies $\Delta y_m \sim \alpha^{-1}$. Coupling this requirement with the choices of α discussed above in different scenarios, we require that the total number of mesh points involved in the calculation of the global solution $n = N_x N_y N_z$ be proportional to N , i.e. $n \sim N$. Having determined the scaling of n , we next present the expression for the computational cost of the global solution t_g as follows:

$$t_g \sim \frac{n}{N_x} O(N_x \log N_x) + \frac{n}{N_z} O(N_z \log N_z) + \frac{n}{N_y} (O(N_y) + O(N_y \log N_y)), \quad (66)$$

where the first two terms on the right hand side denote the cost associated with the FFT operations in x and z directions respectively, while the last term is associated with the cost of the Chebyshev-tau solver in the wall normal y direction. Note that the $O(N_y)$ cost in the expression for the Chebyshev-tau solver is associated with the quasi-tridiagonal solve, while $O(N_y \log N_y)$ cost is associated with the computation of the Chebyshev transforms and its inverse with FFTs. Simplifying the above expression and noting that $n \sim N$, we obtain the following asymptotic scaling

$$t_g \sim n \log n \sim N \log N. \quad (67)$$

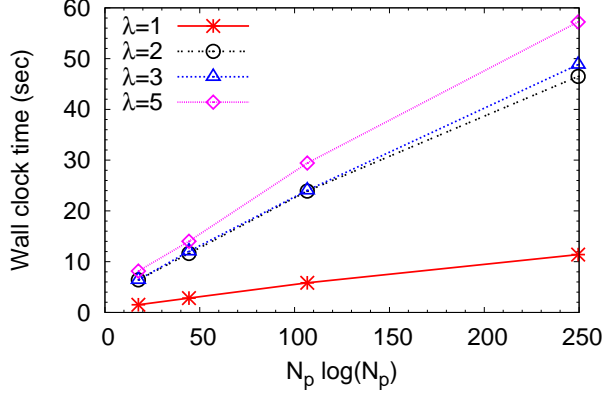


Figure 14: Wall clock time per timestep of a two stage midpoint method for various viscosity ratios λ and for various system sizes. The four data points in the plot correspond to $N_p = 15, 30, 60$, and 120 respectively. Note that the time is plotted against $N_p \log N_p$.

The overall cost per iteration of step 1 or of step 2 is therefore,

$$t = t_l + t_g \sim O(N) + O(N \log N) \sim N \log N. \quad (68)$$

The total cost of step 1 is the cost per iteration times the number of iterations required for convergence. Now, if the number of iterations in step 1 is independent of N , then the computational cost of the overall algorithm will scale as $N \log N$. On the other hand, if the number of iterations in step 1 is dependent on the system size, say it scales as N^e , then the computational cost of the overall algorithm will scale as:

$$t \sim N^{1+e} \log N. \quad (69)$$

Note that the need for iterative solution of step 1 (or a related second kind integral equation) is not unique to the present formulation but is a general feature of any accelerated boundary integral method with $\lambda \neq 1$.

Having determined the expected scaling of our algorithm, we next report timing results from the detailed numerical simulations presented in Sec. 6.1. All runs were performed on a single core of a eight core machine with a 2 GHz Intel Xeon processor running Linux. We plot the time required per stage of the two stage midpoint time stepping algorithm in Fig. (14). Note that the abscissa in the plot is $N_p \log N_p$; the four data points in this plot are respectively for $N_p = 15$, $N_p = 30$, $N_p = 60$ and $N_p = 120$ as discussed above. One can conclude from this plot that in all cases the computational cost scales approximately as $t \sim N_p \log N_p$ (in fact, in this case, the increase in the computational cost appears to be slower than the expected $N_p \log N_p$). Another important feature to note in the plot is the jump in computational cost as one moves from a matched viscosity problem to a non-matched one, which is expected as no iterations are required in matched viscosity problems. The number of iterations required for convergence was found to be independent of the

system size for problems considered here, though it was found to increase with increasing λ . The simulations for $\lambda = 2$ and $\lambda = 3$ capsules required approximately 2 iterations on an average, while the simulation for $\lambda = 5$ capsules required approximately 3 iterations. To summarize this section, we note that a near perfect scaling of $N \log N$ is obtained for both matched viscosity and non-matched viscosity problems. A few words of caution are necessary here, though, as at higher volume fractions and/or at much larger system sizes, the number of iterations for convergence is expected to become system size dependent. It must be emphasized here that this aspect is not specific to our implementation, but is intrinsic to the boundary integral equation for non-matched viscosity problems. Future work on enhancements in the algorithm should address this by the development of efficient preconditioners. Another obvious enhancement in the algorithm will be its parallelization to take advantage of cheaply available multicore processors.

7. Conclusions

A new accelerated boundary integral method for multiphase Stokes flow in a confined geometry was presented. The complexity of the method scales as $O(N \log N)$ for the slit geometry discussed in the present paper. The acceleration in the method was provided by the use of General Geometry Ewald-like (GGEM) method for fast computation of the solution associated with a given collection of point forces. Due to non-periodic nature of the domain, an alternative boundary integral formulation was employed necessitated by the requirements of the acceleration technique. An efficient methodology was presented to compute the resulting double and single layer integrals using the GGEM technique. The resulting implementation was validated with several test problems. The computational complexity of the algorithm was verified to be $O(N \log N)$ with timing results from several large scale multiparticle simulations.

Acknowledgments

The authors gratefully acknowledge Pratik Pranay, Yu Zhang and Juan Hernandez-Ortiz for helpful discussions on the implementation of GGEM. This work was supported by NSF Grant CBET-0852976.

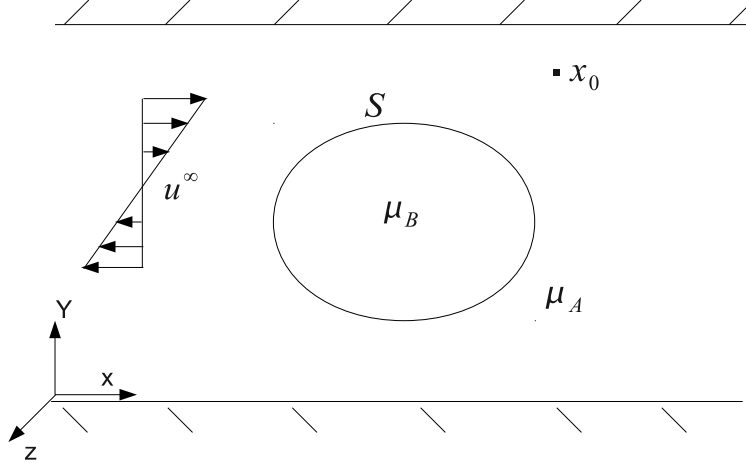


Figure 15: A schematic of the problem for Sec. (Appendix A). The figure shows the dispersed phase with viscosity μ_A and a particle with viscosity μ_B . The surface of the particle is denoted by S . Also shown is the undisturbed flow denoted by \mathbf{u}^∞ .

Appendix A. Derivation of Boundary Integral equation

Consider a two phase flow in a specified geometry as shown in Fig. (1). The two fluids are respectively denoted by A and B in the figure with viscosity μ_A and μ_B . The fluid B is assumed to be enclosed by an impermeable interface denoted by S , which has its own characteristic properties (e.g. drops, capsules, vesicles, etc). Now, consider a point \mathbf{x}_0 in fluid A as shown in Fig. (15). Applying the reciprocal theorem to the disturbance velocity in the region A denoted by $\mathbf{u}^{DA} = \mathbf{u}^A - \mathbf{u}^\infty$, and that due to a point force located at \mathbf{x}_0 , we obtain

$$u_j^{DA}(\mathbf{x}_0) = \frac{-1}{8\pi\mu_A} \int_S f_i^{DA}(\mathbf{x}) G_{ij}(\mathbf{x}, \mathbf{x}_0) dS(\mathbf{x}) + \frac{1}{8\pi} \int_S u_i^{DA}(\mathbf{x}) T_{ijk}(\mathbf{x}, \mathbf{x}_0) n_k(\mathbf{x}) dS(\mathbf{x}), \quad (\text{A.1})$$

where \mathbf{f}^{DA} is the hydrodynamic traction at the interface on the side of fluid A associated with the velocity field \mathbf{u}^{DA} , while \mathbf{G} is the Green's function for the specified geometry and \mathbf{T} is the associated stress tensor. Next, employing the self-adjointness property of the Green's function \mathbf{G} , we obtain the following form of the above equation

$$u_j^{DA}(\mathbf{x}_0) = \frac{-1}{8\pi\mu_A} \int_S f_i^{DA}(\mathbf{x}) G_{ji}(\mathbf{x}_0, \mathbf{x}) dS(\mathbf{x}) + \frac{1}{8\pi} \int_S u_i^{DA}(\mathbf{x}) T_{ijk}(\mathbf{x}, \mathbf{x}_0) n_k(\mathbf{x}) dS(\mathbf{x}). \quad (\text{A.2})$$

Recall that the self-adjointness of the Green's function \mathbf{G} implies that

$$G_{ij}(\mathbf{x}, \mathbf{x}_0) = G_{ji}(\mathbf{x}_0, \mathbf{x}). \quad (\text{A.3})$$

Next, we apply the reciprocal theorem to the undisturbed flow \mathbf{u}^∞ in region B and due to a point force located at \mathbf{x}_0 in region A . This yields,

$$0 = \int_S f_i^{B\infty}(\mathbf{x}) G_{ji}(\mathbf{x}_0, \mathbf{x}) dS(\mathbf{x}) - \mu_B \int_S u_i^\infty(\mathbf{x}) T_{ijk}(\mathbf{x}, \mathbf{x}_0) n_k(\mathbf{x}) dS(\mathbf{x}) \quad (\text{A.4})$$

Note that in the above equation, the normal \mathbf{n} is pointing out of region B into region A (outward normal). We next note the following relation between $\mathbf{f}^{A\infty}$ and $\mathbf{f}^{B\infty}$

$$\frac{\mathbf{f}^{B\infty}}{\mu_B} = \frac{\mathbf{f}^\infty}{\mu_A}. \quad (\text{A.5})$$

This follows from the continuity of the undisturbed flow across the interface, and that the internal and external stresses are computed with viscosity μ_B and μ_A respectively for the same flow field. Using this relationship, we write Eq. (A.4) as

$$0 = -\frac{1}{8\pi\mu_A} \int_S f_j^{A\infty}(\mathbf{x}) G_{ji}(\mathbf{x}_0, \mathbf{x}) dS(\mathbf{x}) + \frac{1}{8\pi} \int_S u_i^\infty(\mathbf{x}) T_{ijk}(\mathbf{x}, \mathbf{x}_0) n_k(\mathbf{x}) dS(\mathbf{x}). \quad (\text{A.6})$$

Adding Eqs. (A.2) and (A.6), we obtain

$$8\pi\mu_A u_j^{DA}(\mathbf{x}_0) = -\int_S f_i^A(\mathbf{x}) G_{ji}(\mathbf{x}_0, \mathbf{x}) dS(\mathbf{x}) + \mu_A \int_S u_i^A(\mathbf{x}) T_{ijk}(\mathbf{x}, \mathbf{x}_0) n_k(\mathbf{x}) dS(\mathbf{x}). \quad (\text{A.7})$$

Next, we apply reciprocal theorem to the fluid velocity in region 2 (\mathbf{u}^B) and due to a point force located at \mathbf{x}_0 . This yields

$$0 = \int_S f_j^B(\mathbf{x}) G_{ji}(\mathbf{x}_0, \mathbf{x}) dS(\mathbf{x}) - \mu_B \int_S u_i^B(\mathbf{x}) T_{ijk}(\mathbf{x}, \mathbf{x}_0) n_k(\mathbf{x}) dS(\mathbf{x}). \quad (\text{A.8})$$

For interfacial flows neither the interfacial velocity nor the interface tractions on either side is known, though we have the following boundary conditions at any point on the interface

$$\mathbf{u}^A = \mathbf{u}^B = \mathbf{u}^I \quad (\text{A.9a})$$

$$\Delta f = \mathbf{f}^A - \mathbf{f}^B = -\mathbf{f}^I, \quad (\text{A.9b})$$

which essentially implies the continuity of the velocity across the interface and that the net force on an element due to hydrodynamic stresses is balanced by the net force due to interfacial stresses, see Sec. (3). We note that the interfacial contribution \mathbf{f}^I is assumed to be known by the known constitutive equation of the interface and its known configuration. Given the unknowns and the boundary conditions, a very common approach is to eliminate the unknown hydrodynamic interfacial tractions \mathbf{f}^A and \mathbf{f}^B with the known traction jump Δf in Eqs. (A.7) and (A.8). This leads to the widely employed second kind integral equation for the unknown interfacial velocity. Here, we adopt an alternative approach. Using Eqs (A.7) and (A.8) we instead eliminate the double layer integral to obtain

$$8\pi\mu_j^{DA}(\mathbf{x}_0) = -\frac{1}{\mu_A} \int_S f_i^A(\mathbf{x}) G_{ji}(\mathbf{x}_0, \mathbf{x}) dS(\mathbf{x}) + \frac{1}{\mu_B} \int_S f_i^B(\mathbf{x}) G_{ji}(\mathbf{x}_0, \mathbf{x}) dS(\mathbf{x}). \quad (\text{A.10})$$

The above can be written in the following form

$$u_j(\mathbf{x}_0) = u_j^\infty(\mathbf{x}_0) + \frac{1}{8\pi} \int_S \left(\frac{f_i^B(\mathbf{x})}{\mu_B} - \frac{f_i^A(\mathbf{x})}{\mu_A} \right) G_{ji}(\mathbf{x}_0, \mathbf{x}) dS(\mathbf{x}). \quad (\text{A.11})$$

This equation for the velocity can be shown to be valid inside, outside, as well as on the boundary S . The drawback of this equation is that both the velocity (including interfacial velocity) and the surface tractions are unknown. The main advantage for our purposes here is that we have switched the pole and the field point of the Green's function using its self-adjointness property (Eq. A.3). For simplifying the notation, we next express the operand of the Green's function by \mathbf{q} , i.e. we define \mathbf{q} as

$$\mathbf{q}(\mathbf{x}) = \frac{1}{8\pi} \left(\frac{\mathbf{f}^B(\mathbf{x})}{\mu_2} - \frac{\mathbf{f}^A(\mathbf{x})}{\mu_1} \right). \quad (\text{A.12})$$

Using the above definition, we write the velocity as

$$u_j(\mathbf{x}_0) = u_j^\infty(\mathbf{x}_0) + \int_S q_i(\mathbf{x}) G_{ji}(\mathbf{x}_0, \mathbf{x}) dS(\mathbf{x}). \quad (\text{A.13})$$

The pressure associated with the above velocity field in the region external to S can be written as

$$p(\mathbf{x}_0) = p^\infty(\mathbf{x}_0) + \mu_A \int_S q_i(\mathbf{x}) P_i(\mathbf{x}_0, \mathbf{x}) dS(\mathbf{x}). \quad (\text{A.14})$$

Using Eqs. (A.13) and (A.14), we can write the stress $\sigma_{jk}^A(\mathbf{x}_0)$ as

$$\sigma_{jk}^A(\mathbf{x}_0) = \sigma_{jk}^{A\infty}(\mathbf{x}_0) + \mu_A \int_S q_i(\mathbf{x}) T_{jik}(\mathbf{x}_0, \mathbf{x}) dS(\mathbf{x}) \quad (\text{A.15})$$

A similar expression can be written for $\sigma_{jk}^B(\mathbf{x}_0)$ as shown below:

$$\sigma_{jk}^B(\mathbf{x}_0) = \sigma_{jk}^{B\infty}(\mathbf{x}_0) + \mu_B \int_S q_i(\mathbf{x}) T_{jik}(\mathbf{x}_0, \mathbf{x}) dS(\mathbf{x}) \quad (\text{A.16})$$

We will now take the limit of the above equations as we approach the interface from either side and then dot it with the normal to get the tractions on either side of the interface \mathbf{f}^A and \mathbf{f}^B . We can express both of them using the principal value of the double layer integral along with the jump condition to obtain [35]

$$f_j^A(\mathbf{x}_0) = f_j^{A\infty}(\mathbf{x}_0) - 4\pi\mu_A q_j(\mathbf{x}_0) + \mu_A n_k(\mathbf{x}_0) \int_S^{PV} q_i(\mathbf{x}) T_{jik}(\mathbf{x}_0, \mathbf{x}) dS(\mathbf{x}), \quad (\text{A.17a})$$

$$f_j^B(\mathbf{x}_0) = f_j^{B\infty}(\mathbf{x}_0) + 4\pi\mu_B q_j(\mathbf{x}_0) + \mu_B n_k(\mathbf{x}_0) \int_S^{PV} q_i(\mathbf{x}) T_{jik}(\mathbf{x}_0, \mathbf{x}) dS(\mathbf{x}), \quad (\text{A.17b})$$

where PV implies the principal value of the improper integral when the observation point lies on the domain of the integration. Note that the sign of the jump condition ($4\pi q_j(\mathbf{x}_0)$) depends on the direction from which we approach the interface relative to the outward normal defined above, i.e. whether we approach the interface parallel to the normal or anti to it.

Taking the difference of Eqs. (A.17a) from (A.17b) and using Eqs. (A.9b) and (A.5), we have that

$$-\Delta f_j(\mathbf{x}_0) = (\lambda - 1)f_j^{A\infty}(\mathbf{x}_0) + 4\pi\mu_A(\lambda + 1)q_j(\mathbf{x}_0) + (\lambda - 1)\mu_A n_k(\mathbf{x}_0) \int_S^{PV} q_i(\mathbf{x}) T_{jik}(\mathbf{x}_0, \mathbf{x}) dS(\mathbf{x}), \quad (\text{A.18})$$

where we have now introduced the viscosity ratio $\lambda = \mu_B/\mu_A$. Rearranging the above equation, we obtain

a second kind integral equation for the density of the Green's function \mathbf{q} as follows:

$$q_j(\mathbf{x}_0) + \frac{\kappa}{4\pi} n_k(\mathbf{x}_0) \int_S^{PV} q_i(\mathbf{x}) T_{jik}(\mathbf{x}_0, \mathbf{x}) dS(\mathbf{x}) = -\frac{1}{4\pi\mu_A} \left(\frac{\Delta f_j(\mathbf{x}_0)}{\lambda + 1} + \kappa f_j^{A\infty}(\mathbf{x}_0) \right), \quad (\text{A.19})$$

where we have defined κ as

$$\kappa = \frac{\lambda - 1}{\lambda + 1}. \quad (\text{A.20})$$

The above equation is used to solve for the unknown density \mathbf{q} , which upon substitution in Eq. (A.13) gives the velocity at any point in the domain, including the interface.

Appendix B. Undisturbed flow stress

For pressure driven flows, the stress tensor is given by

$$\sigma_{ij}^\infty = \frac{8\mu U_0}{H^2} x \delta_{ij} + \frac{4\mu U_0}{H} \left(1 - \frac{2y}{H}\right) e_{ij}, \quad (\text{B.1})$$

where e_{ij} is

$$\mathbf{e} = \begin{pmatrix} 0 & 1 & 0 \\ 1 & 0 & 0 \\ 0 & 0 & 0 \end{pmatrix}. \quad (\text{B.2})$$

Note that the velocity and pressure field in pressure driven flows is given by the following expressions

$$u = 4U_0 \frac{y}{H} \left(1 - \frac{y}{H}\right), \quad (\text{B.3a})$$

$$p = -\frac{8\mu U_0}{H^2} x. \quad (\text{B.3b})$$

In the above equations, U_0 is the centerline velocity. The surface traction $\mathbf{f}^\infty(\mathbf{x})$ can be obtained at a point \mathbf{x} on the surface with normal vector $\mathbf{n}(\mathbf{x})$ as

$$f_i^\infty(\mathbf{x}) = \sigma_{ij}^\infty(\mathbf{x}) n_j(\mathbf{x}). \quad (\text{B.4})$$

For simple shear flows, the stress tensor is given by

$$\sigma_{ij}^\infty = \mu \dot{\gamma} e_{ij}, \quad (\text{B.5})$$

where $\dot{\gamma}$ is the shear rate. The surface traction for this case can be obtained by substituting the stress tensor in the above equation in Eq. (B.4).

Appendix C. Fast Spectral Stokes Flow Solver

Here we discuss the solution procedure for the global problem in Eq. (10) for a slit geometry (Fig. 1). We simplify the notation in Eq. (10) and represent it by the following set of equations:

$$-\nabla p(\mathbf{x}) + \mu \nabla^2 \mathbf{u}(\mathbf{x}) = \mathbf{f}(\mathbf{x}), \quad (\text{C.1a})$$

$$\nabla \cdot \mathbf{u}(\mathbf{x}) = 0, \quad (\text{C.1b})$$

where p is the pressure, $\mathbf{u} = (u, v, w)$ is the velocity, while $\mathbf{f}(\mathbf{x}) = (f_x, f_y, f_z)$ is a known function obtained from the known distribution of global force densities. The above set of equations are supplemented by the periodic boundary conditions in x and z directions, while a Dirichlet boundary condition for the velocity is specified in the y direction:

$$\mathbf{u}(x, z) = \mathbf{g}_1(x, z) \text{ at } y = 0, \quad (\text{C.2a})$$

$$\mathbf{u}(x, z) = \mathbf{g}_2(x, z) \text{ at } y = H. \quad (\text{C.2b})$$

The velocity and pressure variables are first expanded in truncated Fourier series in x and z directions as:

$$u(\mathbf{x}) = \sum_{l=-N_x/2}^{N_x/2-1} \sum_{m=-N_z/2}^{N_z/2-1} \hat{u}_{lm}(y) e^{i2\pi l x/L_x} e^{i2\pi m z/L_z}. \quad (\text{C.3})$$

Similar expressions are written for $v(\mathbf{x})$, $w(\mathbf{x})$, $p(\mathbf{x})$, $f_x(\mathbf{x})$, $f_y(\mathbf{x})$, and $f_z(\mathbf{x})$ by replacing \hat{u}_{lm} by \hat{v}_{lm} , \hat{w}_{lm} , \hat{p}_{lm} , \hat{f}_{xlm} , \hat{f}_{ylm} , and \hat{f}_{zlm} respectively in the above equation. Substituting this in equation (C.1) and employing the Galerkin method, we obtain the following owing to the orthogonality of Fourier modes:

$$-il\hat{p} - \mu(k^2 - \frac{\partial^2}{\partial^2 y})\hat{u} = \hat{f}_x, \quad (\text{C.4a})$$

$$-\frac{\partial \hat{p}}{\partial y} - \mu(k^2 - \frac{\partial^2}{\partial^2 y})\hat{v} = \hat{f}_y, \quad (\text{C.4b})$$

$$-im\hat{p} - \mu(k^2 - \frac{\partial^2}{\partial^2 y})\hat{w} = \hat{f}_z, \quad (\text{C.4c})$$

$$il\hat{u} + \frac{\partial \hat{v}}{\partial y} + im\hat{w} = 0, \quad (\text{C.4d})$$

where we have dropped the subscript lm in the above equation. Next, using the last equation, we eliminate \hat{u} , \hat{v} and \hat{w} in the first three equations to obtain the following equation for the pressure:

$$\frac{\partial^2 \hat{p}}{\partial^2 y} - k^2 \hat{p} = il\hat{f}_x + \frac{\partial \hat{f}_y}{\partial y} + im\hat{f}_z. \quad (\text{C.5})$$

The continuity equation can be replaced by the above equation for pressure along with the boundary condition requiring the velocity to be divergence free [7, 4], i.e.

$$il\hat{u} + \frac{\partial \hat{v}}{\partial y} + im\hat{w} = 0 \text{ at } y = 0 \quad \& \quad y = H. \quad (\text{C.6})$$

Alternatively, one solves the Eq. C.5 with the following pressure boundary condition

$$\hat{p} = \hat{p}_1 \text{ at } y = 0, \quad (\text{C.7a})$$

$$\hat{p} = \hat{p}_2 \text{ at } y = H, \quad (\text{C.7b})$$

though, the pressure boundary conditions above are unknown a priori, but instead they must take a value so that the condition in Eq. (C.6) is satisfied. Grouping all the equations to be solved, we have the following

$$\frac{\partial^2 \hat{p}}{\partial^2 y} - k^2 \hat{p} = i l \hat{f}_x + \frac{\partial \hat{f}_y}{\partial y} + i m \hat{f}_z, \quad (\text{C.8a})$$

$$\mu \frac{\partial^2 \hat{u}}{\partial^2 y} - \mu k^2 \hat{u} - i l \hat{p} = \hat{f}_x, \quad (\text{C.8b})$$

$$\mu \frac{\partial^2 \hat{v}}{\partial^2 y} - \mu k^2 \hat{v} - \frac{\partial \hat{p}}{\partial y} = \hat{f}_y, \quad (\text{C.8c})$$

$$\mu \frac{\partial^2 \hat{w}}{\partial^2 y} - \mu k^2 \hat{w} - i m \hat{p} = \hat{f}_z, \quad (\text{C.8d})$$

with the following boundary conditions

$$\begin{aligned} \hat{p} &= \hat{p}_1, \hat{u} = \hat{g}_{1x}, \hat{v} = \hat{g}_{1y}, \hat{w} = \hat{g}_{1z} \text{ at } y = 0, \\ \hat{p} &= \hat{p}_2, \hat{u} = \hat{g}_{2x}, \hat{v} = \hat{g}_{2y}, \hat{w} = \hat{g}_{2z} \text{ at } y = H, \end{aligned} \quad (\text{C.9})$$

where $\mathbf{g}_1 = (g_{1x}, g_{1y}, g_{1z})$ and $\mathbf{g}_2 = (g_{2x}, g_{2y}, g_{2z})$ and, as with the other quantities, $\hat{\cdot}$ denotes discrete Fourier transform in x and z .

The Kleiser-Schumann influence matrix approach involves solving three set of equations as in Eq. (C.8) with different boundary conditions as discussed shortly. In the first set, one solves the equations in C.8 with the correct boundary conditions for the velocity in Eq. (C.9), but with homogeneous boundary conditions for the pressure, i.e.

$$\hat{p} = 0 \text{ at } y = 0 \text{ \& } y = H \quad (\text{C.10})$$

Each of the equations for pressure and velocity components above are solved here by expanding them in discrete Chebyshev polynomials and then employing the Galerkin method to obtain equations for each of Chebyshev modes. The appropriate boundary conditions are satisfied by employing the tau method [3, 34] in which the equations for the highest two Chebyshev modes are replaced by the boundary condition equations. The solution for pressure is first computed, whose value is then substituted in the equations for velocity. Thus, in each step, one needs to solve a Helmholtz equation using Chebyshev polynomial expansion. In this case, the equations for the unknown Chebyshev coefficients can be reduced to a quasi-tridiagonal matrix equation with the last full row being full, while the rest being in the standard tridiagonal form. Also, note that the equations for the even and odd Chebyshev modes are decoupled and solved separately. These quasi-tridiagonal systems of equations can be solved in $O(N_y)$ time with a direct algorithm [34]. Also, the

use of Chebyshev Gauss-Lobatto quadrature points [3, 34] for transforming a variable between physical and transform space ensures that FFTs can be employed for its evaluation [4]. Therefore, for each of the Fourier modes (l, m) , the asymptotic cost of the Chebyshev-tau solution procedure scales as $N_y \log N_y$. We denote this first set of solution thus obtained for Fourier mode (l, m) by $(\hat{u}_a, \hat{v}_a, \hat{w}_a, \hat{p}_a)$.

The next two sets of equations involve solving the homogeneous version of the differential equations in C.8, i.e., the right hand side of the each of the equations in C.8 is set to zero. Moreover, the velocity boundary condition for these two sets of problems are also homogeneous. The only non-homogeneous equation in these two problems are the pressure boundary conditions. In the first of these, the pressure boundary condition is the following:

$$\hat{p}(0) = 1 \quad \& \quad \hat{p}(H) = 0, \quad (\text{C.11})$$

while in the second the pressure boundary condition is

$$\hat{p}(0) = 0 \quad \& \quad \hat{p}(H) = 1. \quad (\text{C.12})$$

We denote these two solutions by $(\hat{u}_b, \hat{v}_b, \hat{w}_b, \hat{p}_b)$, and $(\hat{u}_c, \hat{v}_c, \hat{w}_c, \hat{p}_c)$. It is important to note that the latter two set of equations are to be solved just once at the beginning of the simulation and the results are stored. The overall solution for the velocity and pressure is then obtained as:

$$\begin{aligned} \hat{u} &= \hat{u}_a + \hat{p}_1 \hat{u}_b + \hat{p}_2 \hat{u}_c, \\ \hat{v} &= \hat{v}_a + \hat{p}_1 \hat{v}_b + \hat{p}_2 \hat{v}_c, \\ \hat{w} &= \hat{w}_a + \hat{p}_1 \hat{w}_b + \hat{p}_2 \hat{w}_c, \\ \hat{p} &= \hat{p}_a + \hat{p}_1 \hat{p}_b + \hat{p}_2 \hat{p}_c. \end{aligned} \quad (\text{C.13})$$

It is easy to see that the above solution satisfies both the differential equations as well as the boundary conditions. The only remaining task is therefore to determine the pressure boundary conditions \hat{p}_1 and \hat{p}_2 . This is accomplished by the requiring that the velocity be divergence free at the boundary (Eq. C.6). Thus, one obtains the following equations for the pressure boundary conditions

$$\begin{pmatrix} C_b(0) & C_c(0) \\ C_b(H) & C_c(H) \end{pmatrix} \begin{pmatrix} \hat{p}_1 \\ \hat{p}_2 \end{pmatrix} = - \begin{pmatrix} C_a(0) \\ C_a(H) \end{pmatrix} \quad (\text{C.14})$$

In the above equations, C_a , C_b and C_c are the continuity expression (Eq. C.6) evaluated at the appropriate boundary point, i.e. at $y = 0$ or $y = H$. For example, $C_a(0)$ is given by

$$C_a(0) = il\hat{u}_a(0) + \frac{\partial \hat{v}_a}{\partial y}(0) + im\hat{w}_a(0) \quad (\text{C.15})$$

The 2×2 coefficient matrix in Eq. (C.14) is known as the influence matrix and the resulting matrix equation is trivially solved at a cost of $O(1)$. The solution in Eq. (C.13) gives the Fourier coefficients of the pressure

and velocity as a function of the wall normal coordinate y , which is then employed to obtain the pressure and velocity in the physical space using inverse FFTs.

References

- [1] Barthes-Biesel, D., 2010. Modeling the motion of capsules in flow. *Current Opinion in Colloid & Interface Science*. DOI: 10.1016/j.cocis.2010.07.001.
- [2] Barthes-Biesel, D., Diaz, A., Dhenin, E., 2002. Effect of constitutive laws for two-dimensional membranes on flow-induced capsule deformation. *Journal Of Fluid Mechanics* 460, 211–222.
- [3] Canuto, C., Hussaini, M. Y., Quarteroni, A., Zang, T. A., 2006. *Spectral Methods Fundamentals in Single Domain*. Springer-Verlag.
- [4] Canuto, C., Hussaini, M. Y., Quarteroni, A., Zang, T. A., 2007. *Spectral Methods Evolution to Complex Geometries and Applications to Fluid Dynamics*. Springer-Verlag.
- [5] Charrier, J. M., Shrivastava, S., Wu, R., 1989. Free and constrained inflation of elastic membranes in relation to thermoforming - non-axisymmetric problems. *Journal Of Strain Analysis For Engineering Design* 24, 55–74.
- [6] Deserno, M., Holm, C., 1998. How to mesh up ewald sums. i. a theoretical and numerical comparison of various particle mesh routines. *Journal of Chemical Physics* 109, 7678–7693.
- [7] Deville, M., Kleiser, L., Montigny-Rannou, F., 1984. Pressure and time treatment for chebyshev spectral solution of a stokes problem. *International Journal for Numerical Methods in Fluids* 4, 1149–1163.
- [8] Doddi, S. K., Bagchi, P., 2009. Three-dimensional computational modeling of multiple deformable cells flowing in microvessels. *Physical Review E* 79, 046318.
- [9] Elman, H. C., Silvester, D. J., Wathen, A. J., 2005. *Finite elements and fast iterative solvers: with applications in incompressible fluid dynamics*. Oxford University Press.
- [10] Freund, J. B., 2007. Leukocyte margination in a model microvessel. *Physics of Fluids* 19, 023301.
- [11] Fung, Y. C., 1996. *Biomechanics: Circulation*, 2nd Edition. Springer-Verlag.
- [12] Greengard, L., Kropinski, M. C., Mayo, A., 1996. Integral equation methods for stokes flow and isotropic elasticity in the plane. *Journal of Computational Physics* 125, 403–414.
- [13] Greengard, L., Rokhlin, V., 1987. A fast algorithm for particle simulations. *Journal of Computational Physics* 73, 325–348.
- [14] Griggs, A. J., Zinchenko, A. Z., Davis, R. H., 2007. Low-Reynolds-number motion of a deformable drop between two parallel plane walls. *International Journal of Multiphase Flow* 33, 182–206.
- [15] Hasimoto, H., 1959. On the periodic fundamental solutions of the Stokes equations and their application to viscous flow past a cubic array of spheres. *Journal of Fluid Mechanics* 5, 317–328.
- [16] Hernandez-Ortiz, J. P., de Pablo, J. J., Graham, M. D., 2007. Fast computation of many-particle hydrodynamic and electrostatic interactions in a confined geometry. *Physical Review Letters* 98, 140602.
- [17] Hernandez-Ortiz, J. P., Ma, H., de Pablo, J. J., Graham, M. D., 2008. Concentration distributions during flow of confined flowing polymer solutions at finite concentration: slit and grooved channel. *Korea-Australia Rheology Journal* 20, 143–152.
- [18] Hughes, T. J. R., 1987. *The Finite element method : linear static and dynamic finite element analysis*. Prentice-Hall.
- [19] Janssen, P. J. A., Anderson, P. D., 2007. Boundary-integral method for drop deformation between parallel plates. *Physics of Fluids* 19, 043602.
- [20] Janssen, P. J. A., Anderson, P. D., 2008. A boundary-integral model for drop deformation between two parallel plates with non-unit viscosity ratio drops. *Journal of Computational Physics* 227, 8807–8819.
- [21] Kim, S., Karrila, S. J., 2005. *Microhydrodynamics: Principles and Selected Applications*. Dover Publications.
- [22] Kumar, A., Higdon, J. J. L., 2011. Particle mesh ewald stokesian dynamics simulations for suspensions of non-spherical particles. *Journal of Fluid Mechanics* 675, 297–335.
- [23] Lac, E., Barthés-Biesel, D., Pelekasis, N. A., Tsamopoulos, J., 2004. Spherical capsules in three-dimensional unbounded Stokes flows: effect of the membrane constitutive law and onset of buckling. *Journal of Fluid Mechanics* 516, 303–334.
- [24] Lac, E., Morel, A., Barthés-Biesel, D., 2007. Hydrodynamic interaction between two identical capsules in simple shear flow. *Journal of Fluid Mechanics* 98, 140602.
- [25] Lambert, J. D., 1997. *Numerical Methods for Ordinary Differential Systems: The Initial Value Problem*. John Wiley & Sons Ltd.
- [26] Li, X., Sarkar, K., 2008. Front tracking simulation of deformation and buckling instability of a liquid capsule enclosed by an elastic membrane. *Journal of Computational Physics* 227, 4998–5018.
- [27] Liron, N., 1996. Stokes flow due to infinite arrays of stokeslets in three dimensions. *Journal of Engineering Mathematics* 30, 267–297.
- [28] Liron, N., Mochon, S., 1976. Stokes flow for a stokeslet between two parallel flat plates. *Journal of Engineering Mathematics* 10, 287–303.
- [29] Loewenberg, M., Hinch, E. J., 1996. Numerical simulation of a concentrated emulsion in shear flow. *Journal of Fluid Mechanics* 321, 395–419.
- [30] MacMeccan, R. M., Clausen, J. R., Neitzel, G. P., Aidun, C. K., 2009. Simulating deformable particle suspensions using a coupled lattice-Boltzmann and finite-element method. *Journal of Fluid Mechanics* 618, 13–39.
- [31] Metsi, E., 2000. Large scale simulation of bidisperse emulsions and foams. Ph.D. thesis, University of Illinois at Urbana-Champaign.
- [32] Muldowney, G., Higdon, J., 1995. A spectral boundary element approach to three-dimensional Stokes flow. *Journal of Fluid Mechanics* 298, 167–192.
- [33] Noguchi, H., Gompper, G., 2005. Shape transitions of fluid vesicles and red blood cells in capillary flows. *Proceedings of the National Academy of Sciences, USA* 102, 14159–14164.
- [34] Peyret, R., 2002. *Spectral Methods for Incompressible Viscous Flow*. Springer-Verlag.
- [35] Pozrikidis, C., 1992. *Boundary Integral and Singularity Methods for Linearized Viscous Flow*. Cambridge University Press.

- [36] Pranay, P., Anekal, S. G., Hernandez-Ortiz, J. P., Graham, M. D., 2010. Pair collisions of fluid-filled elastic capsules in shear flow: effects of membrane properties and polymer additives. *Physics of Fluids* 22, 123103.
- [37] Rahimian, A., Veerapaneni, S. K., Biros, G., 2010. Dynamic simulation of locally inextensible vesicles suspended in an arbitrary two-dimensional domain, a boundary integral method. *Journal of Computational Physics* 229, 6466–6484.
- [38] Rallison, J. M., 1981. A numerical study of the deformation and burst of a viscous drop in general shear flows. *Journal of Fluid Mechanics* 109, 465–482.
- [39] Ramanujan, S., Pozrikidis, C., 1998. Deformation of liquid capsules enclosed by elastic membranes in simple shear flow: large deformations and the effect of fluid viscosities. *Journal of Fluid Mechanics* 361, 117–143.
- [40] Saad, Y., 2003. *Iterative Methods for Sparse Linear Systems*. Society for Industrial and Applied Mathematics.
- [41] Silvester, D. J., Wathen, A. J., 1994. Fast iterative solution of stabilised Stokes systems part ii: Using general block preconditioners. *SIAM Journal on Numerical Analysis* 31, 1352–1367.
- [42] Staben, M. E., Zinchenko, A. Z., Davis, R. H., 2003. Motion of a particle between two parallel plane walls in low-reynolds-number Poiseuille flow. *Physics of Fluids* 15, 1711–1733.
- [43] Stone, H. A., Stroock, A. D., Ajdari, A., 2004. Engineering flows in small devices: Microfluidics toward a lab-on-a-chip. *Annual Review of Fluid Mechanics* 36, 381–411.
- [44] Sui, Y., Low, H. T., Chew, Y. T., Roy, P., 2010. A front-tracking lattice Boltzmann method to study flow-induced deformation of three-dimensional capsules. *Computers & Fluids* 39, 499–511.
- [45] Veerapaneni, S. K., Rahimian, A., Biros, G., Zorin, D., 2011. A fast algorithm for simulating vesicle flows in three dimensions. *Journal of Computational Physics* 230, 5610–5634.
- [46] Zhao, H., Isfahani, A. H. G., Olson, L. N., Freund, J. B., 2010. A spectral boundary integral method for flowing blood cells. *Journal of Computational Physics* 229, 3726–3744.
- [47] Zinchenko, A. Z., Davis, R. H., 2000. An efficient algorithm for hydrodynamical interaction of many deformable drops. *Journal of Computational Physics* 157, 539–587.
- [48] Zinchenko, A. Z., Davis, R. H., 2002. Shear flow of highly concentrated emulsions of deformable drops by numerical simulations. *Journal of Fluid Mechanics* 455, 21–62.